Slicing up the San Francisco Bay Area: Block kinematics and fault slip rates from GPS-derived surface velocities

M. A. d'Alessio,[1] I. A. Johanson, and R. Bürgmann
Berkeley Seismological Laboratory, Berkeley, California, USA

D. A. Schmidt
Department of Geological Sciences, University of Oregon, Eugene, Oregon, USA

M. H. Murray
Berkeley Seismological Laboratory, Berkeley, California, USA

Received 26 October 2004; revised 11 February 2005; accepted 10 March 2005; published 16 June 2005.

[1] Observations of surface deformation allow us to determine the kinematics of faults in the San Francisco Bay Area. We present the Bay Area velocity unification (BĀVŪ, "bay view"), a compilation of over 200 horizontal surface velocities computed from campaign-style and continuous Global Positioning System (GPS) observations from 1993 to 2003. We interpret this interseismic velocity field using a three-dimensional block model to determine the relative contributions of block motion, elastic strain accumulation, and shallow aseismic creep. The total relative motion between the Pacific plate and the rigid Sierra Nevada/Great Valley (SNGV) microplate is 37.9 ± 0.6 mm yr^{-1} directed toward N30.4°W ± 0.8° at San Francisco (±2σ). Fault slip rates from our preferred model are typically within the error bounds of geologic estimates but provide a better fit to geodetic data (notable right-lateral slip rates in mm yr^{-1}: San Gregorio fault, 2.4 ± 1.0; West Napa fault, 4.0 ± 3.0; zone of faulting along the eastern margin of the Coast Range, 5.4 ± 1.0; and Mount Diablo thrust, 3.9 ± 1.0 of reverse slip and 4.0 ± 0.2 of right-lateral strike slip). Slip on the northern Calaveras is partitioned between both the West Napa and Concord/Green Valley fault systems. The total convergence across the Bay Area is negligible. Poles of rotation for Bay Area blocks progress systematically from the North America-Pacific to North America-SNGV poles. The resulting present-day relative motion cannot explain the strike of most Bay Area faults, but fault strike does loosely correlate with inferred plate motions at the time each fault initiated.

Citation: d'Alessio, M. A., I. A. Johanson, R. Bürgmann, D. A. Schmidt, and M. H. Murray (2005), Slicing up the San Francisco Bay Area: Block kinematics and fault slip rates from GPS-derived surface velocities, *J. Geophys. Res.*, *110*, B06403, doi:10.1029/2004JB003496.

1. Introduction

[2] The San Francisco Bay Area hosts a complex plate boundary fault system with large, seismogenic faults that pose significant hazard to the local urban population. Faults in the Bay Area are predominantly locked at the surface while steady plate boundary motion continues to deform the surrounding crust. Monitoring this surface deformation allows us to determine block offset and strain accumulation along the faults. Geodetic monitoring of faults in the Bay Area has been a major effort of the scientific community since *Reid* [1910] first formulated the elastic rebound theory. The development of modern survey techniques such as the Global Positioning System (GPS) allows enhanced measurement precision. A number of studies have reported the results of GPS deformation fields and their estimates of the slip distribution on Bay Area faults [*Savage et al.*, 1998; *Freymueller et al.*, 1999; *Savage et al.*, 1999; *Murray and Segall*, 2001; *Prescott et al.*, 2001]. Studies have also used combinations of GPS and terrestrial geodetic measurements to determine distribution of aseismic creep at depth on the Hayward [*Bürgmann et al.*, 2000; *Schmidt et al.*, 2005] and Calaveras [*Manaker et al.*, 2003] faults.

[3] We present a compilation of GPS measurements for the Bay Area showing the interseismic velocity field from

[1]Now at U.S. Geological Survey, Menlo Park, California, USA.

0148-0227/05/2004JB003496$09.00

1993 to 2003. We then interpret these velocities using a three-dimensional block model that considers the motion of regional crustal blocks and elastic strain accumulation about block-bounding faults. We evaluate deformation at a range of scales, including global tectonics, Bay Area wide deformation, the details of fault geometry, and fault connections on the scale of kilometers.

2. GPS Data and Processing

2.1. Data

[4] The Bay Area velocity unification (BĀVŪ, pronounced "bay view") includes campaign GPS data collected by six different institutions (University of California, Berkeley; U.S. Geological Survey; Stanford; University of California, Davis; University of Alaska Fairbanks; California Department of Transportation) from 1993 to 2003. University NAVSTAR Consortium (UNAVCO) archives all of the raw campaign data (http://archive.unavco.org) and the Northern California Earthquake Data Center (NCEDC) archives the continuous BARD network (http://quake.geo.berkeley.edu/bard/). Transient deformation from the 1989 Loma Prieta earthquake decayed to near zero by 1993 [*Segall et al.*, 2000], so this time period captures relatively steady interseismic strain accumulation.

2.2. GPS Processing

[5] We process GPS data using the GAMIT/GLOBK software package developed at the Massachusetts Institute of Technology and the Scripps Institution of Oceanography (SIO) [*King and Bock*, 2002; *Herring*, 2002]. We include five global stations from the International GPS Service (IGS) network and four to six nearby continuous stations from the BARD network in each of our processing runs. We combine daily ambiguity-fixed, loosely constrained solutions using the Kalman filter approach implemented by GLOBK [*Herring*, 2002]. We include data processed locally as well as solutions for the IGS and BARD networks processed by Scripps Orbit and Permanent Array Center (SOPAC) at SIO (http://sopac.ucsd.edu/). Using the Kalman filter, we combine daily solutions into monthly average solutions, giving each daily solution equal weight. We then estimate the average linear velocity of each station in the network from these monthly solutions. We translate and rotate the final positions and velocities of 23 IGS stations to their best fit values in the ITRF2000 no net rotation global reference frame [*Altamimi et al.*, 2002]. We then rotate the velocities into a stable North America reference frame by solving for the best fitting relative pole of rotation shown for the stations shown in Figure 1. We scale the errors following the method used by the Southern California Earthquake Center's Crustal Motion Map (version 3.0 team, Southern California Earthquake Center (SCEC) Crustal Motion Model (CMM) 3.0, http://epicenter.usc.edu/cmm3/; R. W. King, personal communication, 2003). We add white noise to the formal uncertainties of all stations with a magnitude of 2 mm yr^{-1} for the horizontal components and 5 mm yr^{-1} for the vertical component. To account for "bench mark wobble," we add Markov process noise to the solutions with a magnitude of 1 mm $yr^{-1/2}$. We also include velocities from SCEC CMM 3.0 (Z.-K. Shen et al., The SCEC Crustal Motion Map, version 3.0, unpublished data, 2003, available at http://www.epicenter.usc.edu/cmm) for several sites in the Parkfield area to provide better coverage in central California.

[6] We show the BĀVŪ GPS data for the Bay Area in Figure 2 (also Table ES1 in the auxiliary material).[1] We prefer to visualize velocities in a local reference frame centered around station LUTZ (a BARD continuous site on the Bay Block, roughly at the BĀVŪ network centroid). This reference frame accentuates the gradient in deformation across the Bay Area. We subtract LUTZ's velocity from all stations and propagate the correlations in uncertainty to calculate the error ellipses.

2.3. No Outlier Exclusion

[7] We include velocities for all stations that have at least four total observations spanning at least three years. At no point during the data processing or modeling do we exclude data that appear to be "outliers" based on initial assumptions about plate boundary motion or model misfit. This ensures that the data truly dictate the model results, and that scatter in the data is treated formally.

3. Block Modeling Methodology

[8] In order to calculate slip along faults at depth from observed surface deformation, we must employ interpretive models. In the following sections, we discuss the physical processes that are represented in our numerical model, including block offset, elastic strain accumulation, and shallow interseismic creep.

3.1. Dislocation Modeling

[9] The San Andreas fault system forms the boundary between the Pacific (PA) plate and the Sierra Nevada/Great Valley block (SNGV). Far from the fault, plate tectonic motions continue at a relatively constant rate. In the Bay Area, most plate boundary faults are presently locked near the surface during the interseismic period, causing the entire region to deform elastically under the influence of this far-field plate motion. One way to represent this system is to imagine that the fault itself is locked near the surface, but continues to slip at depth. *Okada* [1985] presents a useful formulation of the mathematics of this relationship for finite fault segments ("dislocations") in an isotropic, homogeneous, linearly elastic half-space. Okada's equations define the relationship between slip on a given fault segment and surface displacement at each station. To uniquely define this relationship, one must specify the depth at which the fault transitions from the locked behavior near the surface to the deep, continuously slipping dislocation (i.e., the locking depth, LD). The transition could reflect thermally controlled onset of plastic flow [*Sibson*, 1982] or the transition from stable to unstable frictional sliding [*Tse and Rice*, 1986; *Blanpied et al.*, 1995]. Because we use the dislocation as a proxy for steady plate motion, we treat the terms "long-term slip rate" and "deep slip rate" as synonyms.

3.2. Block Modeling

[10] Block modeling is an extension of dislocation modeling, but with the additional physical constraint that

[1] Auxiliary material is available at ftp://ftp.agu.org/apend/jb/2004JB003496.

Figure 1. Observed global GPS velocities shown in a reference frame with stable North America. Only stations included in modeling are shown, but BĀVŪ includes additional global stations for reference frame stabilization. The 95% confidence bound on Pacific-North America relative pole of rotation for the Preferred model is shown as the very small ellipse to the right of the PA-NA label. The 95% confidence ellipses on velocities are shown. Labels show the four-character names of GPS stations from the International GPS Service (IGS) network. See color version of this figure in the HTML.

dislocations form the boundaries of rigid plates, or "blocks" [e.g., *Bennett et al.*, 1996; *Murray and Segall*, 2001; *McCaffrey*, 2002]. The amount of slip along each dislocation is determined by the motion of the entire block, resulting in continuity of slip on adjacent fault segments. Here we use an extension of the block modeling code by *Meade et al.* [2002] (who also have a concise introduction to block modeling) and *Meade and Hager* [2005] (who give the latest formulation of the methodology) that includes deformation from shallow aseismic creep (see section 3.3).

[11] In block modeling, we define blocks on a spherical Earth bounded by faults. Defining the model geometry therefore requires more information than dislocation modeling because the location of fault connections must be known so that the faults form a continuous boundary around every block (section 3.6). Each block rotates about a "rotation axis" passing through the center of the Earth and intersecting the surface at a "pole of rotation" (sometimes referred to as an "Euler pole" [e.g., *Cox and Hart*, 1986]).

[12] For each block in the model, there are only three unknown parameters, the three components of the angular velocity vector, $\boldsymbol{\Omega}$. The slip rates, $\mathbf{s}$, of block bounding faults are directly determined by the relative rotation of the surrounding blocks. We resolve this relative motion onto the orientation of the fault that accommodates the motion, and the ratio between strike-slip, dip-slip, and tensile-slip (fault perpendicular motion) components is controlled exclusively by the fault orientation ($\mathbf{s} = f(\boldsymbol{\Omega}$, fault strike, fault dip).

3.3. Surface Creep

[13] Several faults in the Bay Area exhibit aseismic creep at depths shallower than LD [see *Galehouse and Lienkaemper*, 2003]. To incorporate the effects of near-surface aseismic creep on interseismic surface velocities, we include a shallow dislocation with uniform slip rate, c, that runs from the surface to a certain "transition depth" (TD). The TD must be $\leq$LD because, by definition, the fault slips at a uniform rate below LD. The fault is locked at depths between TD and LD. Because the detailed distribution of creep at depth is not well known on all Bay Area faults, we assume the simplest case where TD = LD (the fault creeps at one uniform rate from the surface to LD, where it transitions to its deep slip rate at all depths below LD). We explore the depth sensitivity of TD in section 5.2. The shallow dislocation representing aseismic creep is completely independent from the block motion and is permitted to slip at any rate slower or faster than the deep slip rate if the data favor such behavior.

[14] For segments where *Galehouse and Lienkaemper* [2003] observe surface creep magnitudes less than 1 mm yr^{-1}, we do not solve for a shallow dislocation and keep the fault completely locked above LD. We only consider strike-slip motion on shallow dislocations, so c is a scalar.

[15] BĀVŪ includes more than 60 stations within 15 km of the Hayward fault, so we solve for 4 different shallow dislocations along strike. However, it is not possible to reliably constrain the surface creep rate for some Bay Area faults with GPS data alone because the stations are not typically located within a few kilometers of the fault. We therefore include the surface slip rates summarized by *Galehouse and Lienkaemper* [2003] as a priori constraints for the shallow slip rates with a priori uncertainties equal to the published uncertainties that include a random walk component. These uncertainties are sufficiently large such that the creep rate is determined largely by GPS data where stations are close enough to a fault to resolve shallow slip.

3.4. Inverse Model

[16] Combining block offset, elastic strain accumulation at block boundaries, and shallow aseismic creep, we solve the following equation in an inverse sense:

$$\mathbf{v}(\mathbf{r}_i) = \boldsymbol{\Omega}_i \times \mathbf{r}_i - \sum_{f=1}^{N_{\text{faults}}} \left[\mathbf{G}_i^f \cdot \mathbf{s}^f(\boldsymbol{\Omega}_i) - \mathbf{G}_{\text{creep},i}^f \cdot c^f \right] \qquad (1)$$

where $\mathbf{v}$ is the predicted surface deformation rate, $\mathbf{r}_i$ is the position of station i on Earth, the first term on the right-hand side (cross product term) represents rigid rotation due to the angular velocity of the block, the second term (summation term) represents elastic strain related to fault slip on each segment. $\mathbf{G}_i^f$ and $\mathbf{G}_{\text{creep},i}^f$ are Green's functions relating slip on fault f to deformation at station i for the deep dislocation (slip below LD) and shallow dislocation (between TD and the surface), respectively. Unlike the deep slip rate, $\mathbf{s}$, that is a function of the block rotation, $\boldsymbol{\Omega}$, the shallow creep rate, c,

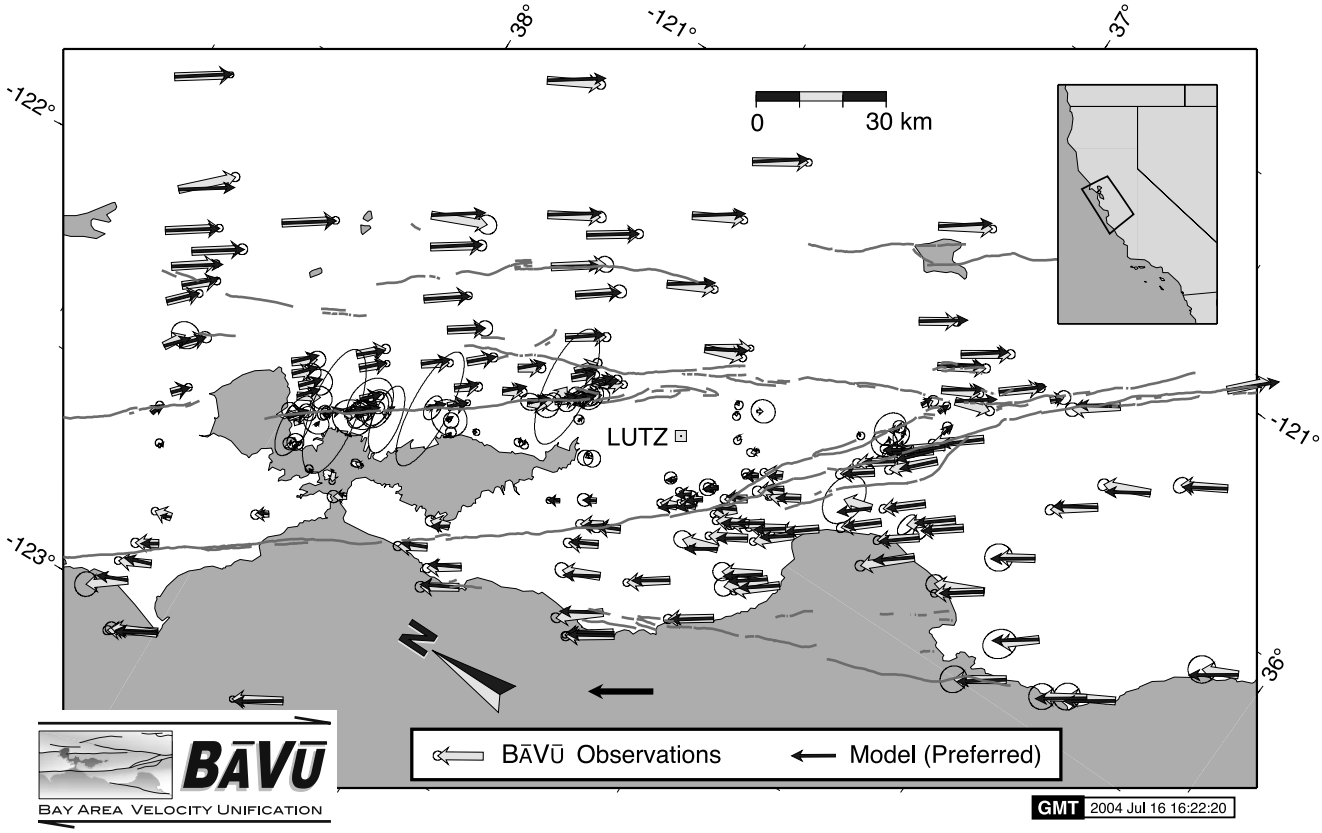

Figure 2. BĀVŪ data set on map of the San Francisco Bay Area with GPS velocities from 1993 to 2003 relative to station LUTZ on the Bay Block. The map projection is about the Pacific Plate-Sierra Nevada/Great Valley (PA-SNGV) pole of rotation, so velocities along a small circle path predicted from the rotation axis of the PA-SNGV block rotation show up as horizontal vectors. We compare observations (wider vectors with 95% confidence error ellipses) with predictions from our Preferred model (narrow, darker vectors). See color version of this figure in the HTML.

is a new model parameter that must be estimated. We solve for the value of $\boldsymbol{\Omega}$ for each block and c for each creeping fault segment that predicts a velocity field most consistent with our observations.

3.5. Inclusion of Global Data

[17] We incorporate data from throughout the Pacific (PA) and North American (NA) plates to determine the total magnitude of relative motion that must be accommodated by Bay Area faults. As long as the assumption that the plates behave rigidly in their interiors is valid, global data far from faults provide valuable constraints. (Strictly speaking, we treat the blocks as purely elastic. Because the blocks are so large, points near the plate interior are virtually unaffected by elastic strain at the block boundaries. Hence we refer to block interiors as "rigid.") Figure 1 shows the distribution of global stations that we include in our analysis.

[18] Our block geometry includes a boundary between the SNGV and NA plates along the Eastern California Shear Zone (ECSZ) (Figure 3). While the SNGV block is thought to behave "rigidly" [*Argus and Gordon*, 1991], the Basin and Range between eastern California and the Colorado Plateau is an area of distributed deformation [*Thatcher et al.*, 1999; *Bennett et al.*, 2003]. We do not include data from within the Basin and Range, so we are insensitive to the details of how deformation is distributed across it. Our ECSZ boundary is therefore a proxy for the total deformation in the Basin and Range between the SNGV and stable North America.

3.6. Fault Geometry

[19] Recent geologic and geomorphic mapping efforts throughout the Bay Area, and especially in the northern East Bay Area, provide new constraints on the details of fault geometry. We define faults in our model using a combination of several data types: (1) mapped surface traces of faults; (2) relocated microseismicity; (3) topographic lineaments; and (4) interpreted geologic cross sections. Figure 4 and auxiliary material Table ES2 show model fault segments presented in this manuscript and Table 1 describes the variations we discuss. We include models that range in complexity from intentionally oversimplified (such as "TwoPlate") to those that are likely beyond the resolving power of our data ("Complex").

4. Results

[20] We evaluated nearly 100 different variations on fault geometry to determine the models most consistent with the geodetic data and mapped faults. We report only a

small subset of these models, highlighting the key parameters that affect model fit. Changes in model geometry (including fault connections, location, orientation, LD, and TD) can affect the inferred fault slip rates greater than indicated by the formally propagated uncertainties from the inverse problem, which are typically <1.5 mm yr^{-1} at the 95% confidence level. For the range of reasonable geometries we test, the slip rates on almost all faults are within ±3 mm yr^{-1} of the Preferred model, which we consider to be representative of the actual confidence interval of our slip rate estimates. For quantitative comparisons, we restrict our analyses to the formal uncertainties, but note that this variation should be considered when interpreting our results.

[21] Figures 2 and 3 show observed and modeled GPS velocities for our Preferred model at the scale of all the Bay Area and California, respectively. Overall, the model predictions agree quite well with the observations and we capture many of the details of deformation across the Bay Area. Examining the "residuals," allows a more detailed comparison of the systematic differences between observations and predictions for several model variations (Figure 5).

[22] We quantify the goodness of fit in terms of the χ^2 and χ^2/DOF statistics:

$$\chi^2 = \sum_{c=1}^{N_{\text{data}}} \left(\frac{v_c^{\text{model}} - v_c^{\text{data}}}{\sigma_c} \right)^2 \tag{2}$$

$$\chi^2/\text{DOF} = \frac{\chi^2}{N_{\text{data}} - N_{\text{model}}} \tag{3}$$

where v_c^{model} and v_c^{data} are the predicted and observed velocity components and σ_c is the 1σ uncertainty for each component of the input GPS velocities. The number of degrees of freedom (DOF) is defined by N_{data}, the number of GPS components used as input data (east and north component for each station, as well as any a priori constraints), and N_{model}, the number of model parameters that we solve for in the inversion (pole of rotation latitude, longitude, and rotation rate, as well as shallow creep rate for creeping segments). These statistics indicate how well the models fit the data within their uncertainty bounds. Lower values of χ^2 indicate a better fit to the data. Increasing the number of model parameters inevitably leads to better fits and lower total χ^2. Dividing by the number of degrees of freedom (DOF) helps us compare models where we solve for a different number of free parameters, but χ^2/DOF ignores all correlations between parameters. Because these correlations change as model geometry changes, caution should be exercised in making strictly quantitative comparisons of models using χ^2/DOF alone. Nonetheless, the statistics do provide a basis for qualitative comparisons. For uncorrelated model parameters, a χ^2/DOF of 1 indicates that on average, all the predicted velocities are consistent with the 1σ standard deviation of the input data. In Table 2, we present misfit statistics for the models we discuss. We typically obtain χ^2/DOF of 3–4, which is partly the result of the χ^2 statistic's strong sensitivity to outliers.

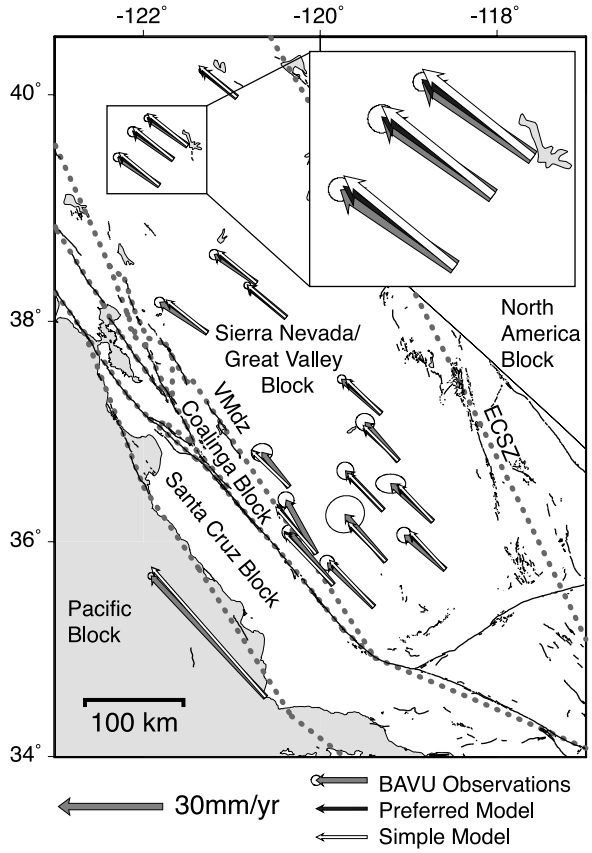

Figure 3. GPS observations within California, shown in a reference frame with stable North America (wide vectors with error ellipses) compared with model results (narrow vectors). Dark sinuous lines are Holocene active faults. Dotted gray lines show a representative model geometry from our Complex model that includes all segments. We label select blocks and faults outside the Bay Area. VMdz, Valley Margin deformation zone; ECSZ, Eastern California Shear Zone. Inset shows an enlargement of the area where the two models differ most in the northern section of the figure. Our Preferred model with a VMdz (darker vectors) fits the data better than models that exclude this fault (Simple model, white vectors). See color version of this figure in the HTML.

[23] In the following sections, we look in detail at the model results at a range of scales from global motions to the details of fault connections and step overs.

4.1. Global Plate Motion

[24] To verify that our block model provides valid constraints on the total relative plate motion, we compare them with previously published results in auxiliary material Table ES3. Our estimates of relative rotation axes incorporate the effect of elastic strain accumulation while the previous studies of block motion typically exclude data from near plate boundaries. To verify the quality of the BAVU global velocities, we use our block modeling code and the identical subset of stations from *Steblov et al.* [2003]. Our results agree almost identically to their published results, though our propagated uncer-

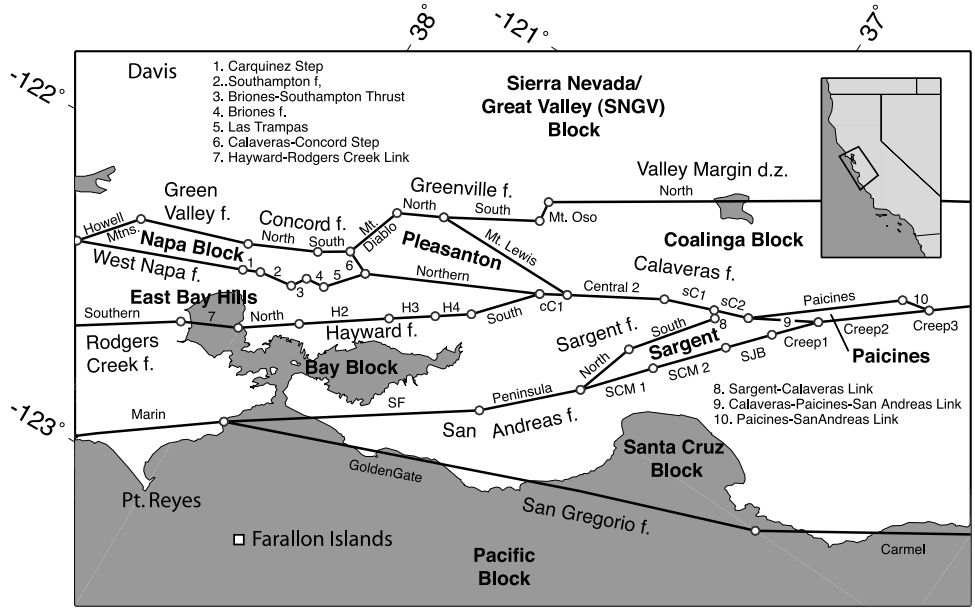

Figure 4. Model fault segments in the Bay Area. Note that not all segments are used in all model variations. Block names are in large, bold text. Fault names are in larger plain text, and names of subsegments of those faults are in smaller text. Abbreviations are cC, central Calaveras; sC, southern Calaveras; SF, San Francisco; SCM, Santa Cruz Mountains; SJB, San Juan Bautista; f, fault. See also Table ES2. See color version of this figure in the HTML.

tainties are slightly smaller. In our "TwoPlate" model, we include all 21 North American and 6 Pacific sites from BĀVŪ that are further than 100 km from a plate boundary. The pole of rotation from TwoPlate is 1.7° east, 1.3° north, and 0.5% slower than the *Steblov et al.* [2003] pole, but the change is not significant at the 95% confidence level. The estimated pole from our "Preferred" model is about 0.9° east, 1.1° north, and 0.9% slower than the *Steblov et al.* [2003] pole. Globally, our data set and block modeling produce reasonable estimates of block motion.

[25] Locally, the slight changes in the NA-PA rotation axis are insignificant. Table 3 shows the predicted velocity at the Farallon Islands station 36 km west of the San Andreas fault (FARB). The predicted velocities for this Bay Area station differ by less than 0.2 mm yr^{-1} and vary

Table 1. Model Name Abbreviation Key, Listed in Order of Increasing Complexity and Abbreviations for Variations on the Four Main Models

Model	Description
TwoPlate	pure block offset between Pacific and North America; excludes all GPS data in California and near plate boundaries; allows comparison with previous global studies
Simple	includes block offset, strain accumulation, and shallow creep on the major Bay Area faults and ECSZ; slip transfers from the Calaveras to the Greenville fault via the Mount Lewis trend; the Calaveras connects to the Concord/Green Valley system eastward across a right step
Preferred	similar to Simple, but slip on the Greenville fault connects to the "Valley Margin deformation zone" along the eastern edge of the Coast Ranges; no Mount Lewis trend; Calaveras connects to both West Napa fault (westward) and Concord fault (eastward); the Preferred model is our reference for comparison between models and the basis for exploration of geometric variations
Complex	includes all faults in the Preferred model, along with more complex connections between the Calaveras and San Andreas faults, a Sargent fault, and a Mount Lewis trend; this model is probably overly complex given our data resolution
CalaverasWest	forces all slip on the northern Calaveras to transfer in a left-stepping sense (westward) onto the west Napa fault
CalaverasEast	forces all slip on the northern Calaveras to transfer across a right step (eastward) to the Concord fault
LD/TD = 13	sets the locking depth (LD; section 5.1) or transition depth (TD; section 5.2) of all faults in the model equal to a uniform value (in this case, 13 km)
LD/TD = D_{95} + 1	locking depths shifted uniformly up or down from D_{95} values of individual segments by the given amount; note that in our sign convention, +1 is deeper by 1 km, while −1 is closer to the surface
Thrust	dipping Mount Diablo and Mount Oso thrust faults; see section 6.4
Unclamped	relaxes some a priori constraints on fault normal motion; see section 5.3

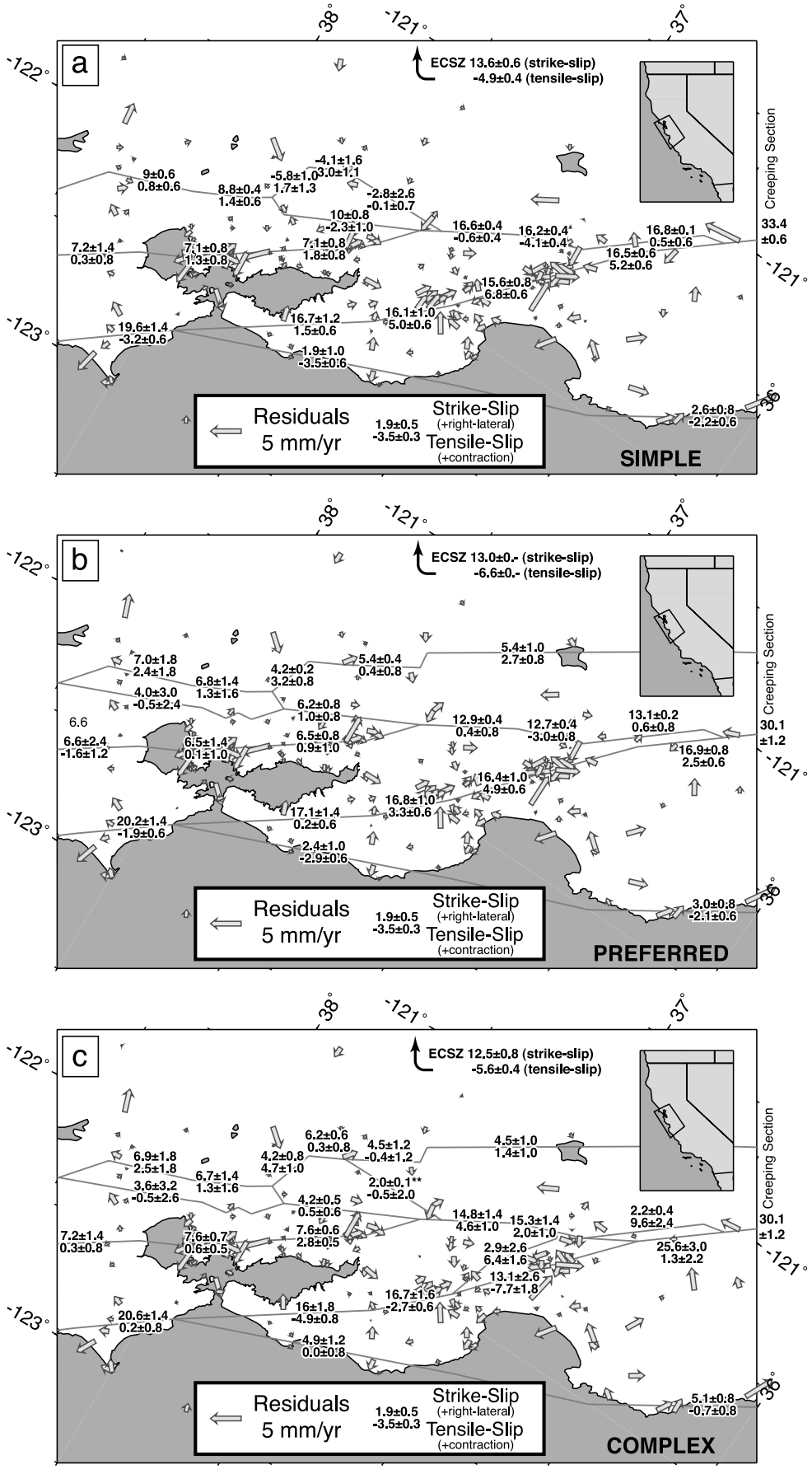
a
ECSZ 13.6±0.6 (strike-slip)
-4.9±0.4 (tensile-slip)
Creeping Section
Residuals
5 mm/yr
1.9±0.5
-3.5±0.3
Strike-Slip
(+right-lateral)
Tensile-Slip
(+contraction)
SIMPLE
b
ECSZ 13.0±0.- (strike-slip)
-6.6±0.- (tensile-slip)
Creeping Section
Residuals
5 mm/yr
1.9±0.5
-3.5±0.3
Strike-Slip
(+right-lateral)
Tensile-Slip
(+contraction)
PREFERRED
c
ECSZ 12.5±0.8 (strike-slip)
-5.6±0.4 (tensile-slip)
Creeping Section
Residuals
5 mm/yr
1.9±0.5
-3.5±0.3
Strike-Slip
(+right-lateral)
Tensile-Slip
(+contraction)
COMPLEX

Figure 5

Table 2. Misfit Statistics for Different Models

Model	χ^2	DOF	χ^2/DOF
TwoPlate[a]	138.9	45	3.09
Simple	2053.8	520	3.95
Preferred	1880.0	517	3.64
Complex	1704.8	510	3.34
Variations on models			
CalaverasWest	1932.5	520	3.72
CalaverasEast	1910.7	520	3.67
Preferred-Thrust	1887.9	517	3.65
Preferred-Unclamped	1871.1	514	3.64
Preferred, LD = D_{95} − 8	1911.9	517	3.70
Preferred, LD = D_{95} − 5	1795.5	517	3.47
Preferred, LD = D_{95} + 5	2053.9	517	3.97
Preferred, LD = 5	1923.0	517	3.72
Preferred, LD = 8	1805.9	517	3.49
Preferred, LD = 13	1875.0	517	3.63
Preferred, LD = 18	2047.1	517	3.96
Preferred, TD = 5	1997.9	517	3.86
Preferred, TD = D_{95}/2	1986.5	517	3.84
Preferred-WG02	3675.7	539	6.82

[a]Note that TwoPlate excludes all data within 100 km of the plate boundary.

in azimuth by less than 0.1°, despite differences in the NA-PA poles.

4.2. Sierra Nevada/Great Valley Block

[26] The Sierra Nevada/Great Valley (SNGV) block is a rigid block that lies at the eastern margin of the Bay Area. The relative motion of the SNGV is not as well constrained as larger plates because of the limited size of the block and relatively sparse data. By including stations from throughout northern and southern California along with strain accumulation near the block boundaries, our block model provides an improved constraint on the total PA-SNGV motion that must be accommodated by Bay Area faults. Table ES3 shows our estimates of the relative motion between PA-SNGV and NA-SNGV compared with previous studies.

[27] In general, the NA-SNGV pole tends to lie southwest of the Bay Area in the Pacific Ocean, as far as 90° from the NA-PA pole (Figure 6). The NA-SNGV poles from previous studies vary by >50° in both longitude and latitude, and our results show a similarly broad range due to slight variations in fault geometry and locking depth. These estimates seem to lie along a consistent azimuth roughly perpendicular to the average fault strike in the San Andreas fault system. The ideal station coverage for determining rotation axes covers a very broad area in all directions. The SNGV and other Bay Area blocks are elongate parallel to the San Andreas system and very narrow perpendicular to it. The orientation of elongated error ellipses for these poles is related to the elongated shape of the blocks. This station geometry also results in a strong trade-off between the rotation rate and distance of the poles of rotation from the Bay Area without strongly influencing predictions of local surface deformation (e.g., Table 3).

[28] The PA-SNGV pole is well constrained and located just west of Lake Superior, ~20° from the NA-PA pole. Unlike NA-SNGV, formal uncertainties for this pole location are <3°, and the best fit estimates vary by only ±6° for a wide range of model geometries. The pole for PA-SNGV is much less affected by the tradeoff between pole position and rotation rate than the NA-SNGV pole.

4.3. Poles of Rotation of Bay Area Blocks

[29] Focusing in on the Bay Area itself, we can examine rotation axes of smaller blocks bounded by Bay Area faults. Figure 6 shows the pole of rotation of each block relative to North America. There is a systematic progression of the poles from west to east. In our Preferred model, the poles form a transition between the NA-SNGV and NA-PA poles. The Santa Cruz block, located adjacent to the Pacific plate, rotates about a pole located near the NA-PA pole. On the other side of the Bay Area, the Coalinga block, located adjacent to the SNGV block, rotates about a pole located very close to the NA-SNGV pole. These blocks near the margins of the Bay Area move very similarly to the larger blocks that bound the region. Blocks within the Bay Area have rotation poles relative to NA in between these poles, with blocks toward the eastern side of the Bay Area tending to move more like NA-SNGV and blocks on the western side moving more like NA-PA. This pattern holds for variations in locking depth and slight variations in geometry on the Preferred model. For the Complex model, the poles of Bay Area blocks are still distributed between the NA-PA and NA-SNGV poles, but the east-west progression breaks down slightly as many of the smaller blocks rotate about poles very close to the blocks themselves.

4.4. Slip Rates on Bay Area Faults

[30] As described in section 3.2, our block model uses GPS observations of surface deformation to calculate the best fitting deep slip rate from given block/fault geometries and locking depths. Here we present a general discussion about the effect of variations in locking depth on estimated slip rates (also see section 5.1), and we present slip rates using our preferred locking depths.

4.4.1. Locking Depth

[31] *Freymueller et al.* [1999] described the strong trade-off between assumed locking depth and calculated slip rate in dislocation models of the San Andreas system, making it challenging to uniquely determine the slip rate on a given fault. We use the maximum depth of seismicity and surface heat flow to gain insight into the depth of the seismic/aseismic transition. Using this depth as a proxy for the geodetic LD helps reduce the ambiguity in determining slip rates. Earthquakes rarely occur below 20 km depth in the Bay Area, and the specific depth where faults become seismically quiet varies spatially throughout the region. Here we document temporal and spatial variation in the depth of seismicity throughout the Bay Area in order to

Figure 5. Residual velocities. Difference between observed GPS velocities and model calculations for three different model scenarios are given. Numbers indicate strike-slip and tensile-slip rates and 95% (2σ) uncertainties for select fault segments. Positive strike slip indicates right-lateral slip. Positive tensile slip indicates contraction, while negative tensile slip indicates extension. See color version of this figure in the HTML.

Table 3. Predicted Magnitude of Velocity at the Farallon Islands (Station FARB) in a Fixed North American Reference Frame[a]

Reference	Rate, mm yr^{-1}	Azimuth, °NW
BĀVŪ observed	47.7 ± 0.8	37.0 ± 1.0
NUVEL-1A	46.5	33.5
SIMPLE	48.0	38.4
PREFERRED	48.0	38.5
COMPLEX	48.2	38.5
Contributions to Preferred model		
Long-term Block Offset	50.7	38.8
Strain Accumulation	−2.9	47.0
Shallow Creep	0.2	80.1
Sum	48.0	38.5

[a]Note that FARB is "slowed" down by ~3 mm yr^{-1} compared to the total rigid plate motion because of elastic strain along Bay Area faults. FARB is far enough from creeping fault segments to be relatively insensitive to their effect. Studies that ignore strain accumulation are not able to reliably predict the velocity at FARB.

accurately determine the seismic/aseismic transition depths.

[32] This transition is commonly quantified by the depth at which 95% of catalog seismicity occurs above and 5% occurs below, or "D_{95}." *Williams* [2003] suggests that D_{95} accurately reflects the deepest extent of rupture in large earthquakes and presents the calculated values of D_{95} for Bay Area fault segments derived from the Northern California Seismic Network (NCSN) catalog. We perform a similar analysis on the high-precision catalog of *Waldhauser and Ellsworth* [2002]. This catalog utilizes relative relocations that have vertical precision of less than about a hundred meters. We divide the Bay Area into a data-driven grid using the quadtree algorithm with a minimum grid cell size of 0.2° [*Townend and Zoback*, 2001]. Figure 7 shows the depth of maximum seismicity for the entire duration of the catalog (1984–2001) and a movie in the auxiliary material shows the time evolution of D_{95}. Since LD is likely thermally controlled, we include heat flow observations for reference. In both illustrations, grid cells are only filled with a color if there are more than 60 events during the time period indicated in the lower left. This number of events seems to produce consistent and stable values for D_{95} [*Magistrale*, 2002].

[33] We do not utilize the D_{95} value as the locking depth for three fault segments. The Marin segment of the San Andreas fault has essentially no seismicity, so we cannot calculate D_{95}. The grid cells south and east of it both have locking depths close to 12 km. However, using a locking depth of 15 km provides a better fit to the geodetic data. D_{95} on the Greenville fault is very deep in the north near Mount Diablo (18 km), but gets much shallower in grid cells to the south (other than the Geysers, these 3 grid cells have the shallowest D_{95} in the Bay Area with values of 8–9 km). A much better fit is achieved if the 18 km locking depth is extended further south along all of the segments, including the fault along the margin of the Great Valley. Heat flow data are sparse in this region, but available data near the Ortigalita fault range from 65 to 85 mW m^2 [*Lachenbruch and Sass*, 1980], values more consistent with a locking depth of 8–12 km, based on the relationships established by *Williams* [1996]. The model preference for a deeper locking depth results in deformation over a broader region surrounding the single block boundary in our model, which could be indicative of a broader deformation zone in this region.

4.4.2. Slip Rates

[34] Deep slip rates determined by our block model are reported in Figure 5 and Table 4 and auxiliary material Table ES4. The total vector sum of relative motion accommodated by Bay Area faults in the Preferred model is 37.9 ± 0.6 mm yr^{-1} oriented at N30.4°W ±0.8° in the central North Bay and at N34.2°W ±0.8° in the central South Bay (rate varies by 1–2 mm yr^{-1} from east to west across the Bay

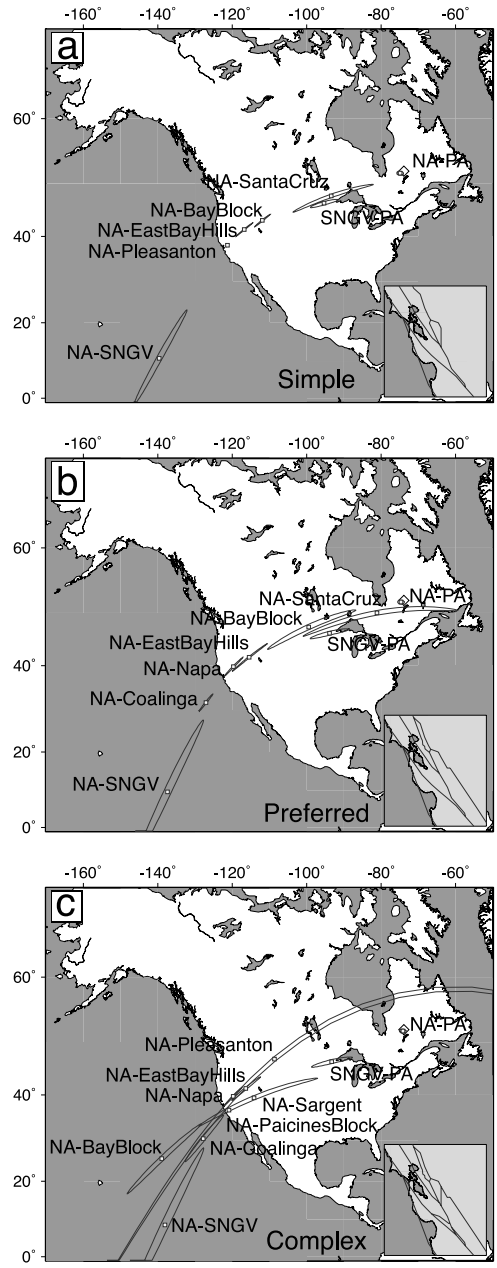

Figure 6. Calculated poles of rotation and 95% confidence limits for blocks in the Bay Area. Other than the Pacific-SNGV pole, all poles are relative to North America (NA). Diamond southeast of Hudson Bay indicates the PA-NA pole for TwoPlate, which excludes data near plate boundaries. See color version of this figure in the HTML.

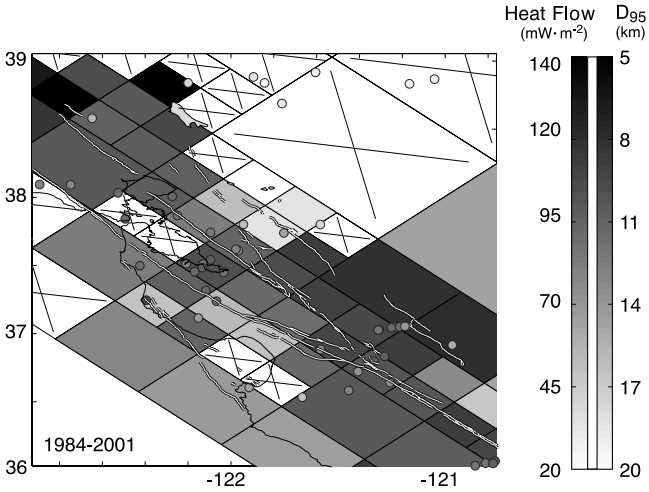

Figure 7. D_{95}, the depth at which 95% of the seismicity in a certain area is above and 5% is below, indicated by shading of rectangular grid cells. D_{95} is calculated from the relative relocation catalog of *Waldhauser and Ellsworth* [2002] with earthquakes from 1984 to 2001. Shaded circles are borehole heat flow measurements from the USGS California heat flow database (http://quake.wr.usgs.gov/heatflow/). The two data sets are plotted using similar color schemes so that shallow D_{95} depths and high heat flows both appear in the same color. While the data sets are often well correlated, the exact relationship depends on rock type and may not be linear as implied by the shared color scheme [*Magistrale*, 2002]. D_{95} is not estimated for grid cells with <60 events (cells with crosses). See color version of this figure in the HTML.

Area, while azimuth varies by up to 8° from north to south). We report slip rate uncertainties at the 95% confidence level (2σ). The sum of best fit slip rates ranges from 31.5 to 39.3 mm yr^{-1} for the different fault geometries and locking depths we have explored. The Simple model consistently produces the lowest total slip rate. Within the Preferred model, the total slip is a strong function of assumed locking depth. The total best fit slip rate ranges from 34.6 to 39.3 mm yr^{-1} as we vary the locking depth over a range of 13 km.

[35] We highlight the slip rates of a few key fault segments. Our model provides a robust estimate of slip on the San Gregorio fault. Because this fault is partly offshore in the Bay Area it is very difficult to estimate a rate using independent dislocations and onshore data. Our block model includes global stations to help constrain the motion of the Pacific block relative to the Bay Area. The resulting slip rate on the San Gregorio fault from our Preferred model is 2.4 ± 1.0 mm yr^{-1} near the Golden Gate, with a slightly higher rate off of Monterey Bay.

[36] We include the West Napa fault in some models, as it may be the northern continuation of the Calaveras fault along a series of westward steps (J. Unruh, personal communication, 2004). We find that its slip rate ranges from 3.4 to 7.4 mm yr^{-1} across all models, with most models estimating slip rates near the lower end of this range. Models where 100% of the slip on the northern Calaveras fault transfers to the West Napa fault produce the higher slip rates. In our Preferred model it slips at 4.0 ± 3.0 mm yr^{-1}. This is the highest formal uncertainty for any deep slip rate in the inversion. In models where the West Napa fault and the Green Valley fault are both allowed to carry some of the Calaveras slip, the slip rates of the two faults sum to 9.5–11.0 mm yr^{-1}, depending on model geometry and locking depth.

[37] Models where we include a fault along the western margin of the Great Valley produce systematically better fits to the data than those that exclude this fault. This fault follows the eastern front of the Coast Ranges, passing along the Ortigalita fault. We find a strike-slip rate of 5.4 ± 1.0 mm yr^{-1} in our Preferred model, and the rate typically varies between 4 and 6 mm yr^{-1}.

4.5. Shallow Creep

[38] Auxiliary material Table ES5 shows the best fit slip rates along dislocations that intersect the surface (surface creep) in our Preferred model. These rates typically vary by <0.5 mm yr^{-1} between most model geometries. Because data coverage is sparse in some areas, the formal uncertainties in creep rates are larger than for the deep slip rates. For the Hayward fault where BĀVŪ has abundant near-fault velocities, the estimated creep rate has the smallest uncertainty (1.2–1.4 mm yr^{-1}). The calculated creep rate variations there are qualitatively similar to the measurements from *Lienkaemper et al.* [2001] and are within about ~1 mm yr^{-1} of their observations even when the a priori constraints are removed.

Table 4. Comparison of Strike-Slip Rates for Geologic Estimates (WGCEP2002) and This Study[a]

	SG		SA			RC/H		C				GV/Gr			
Model	N	S	Mr	SF	SCM	RC	H	WN	N	C	S	GV	Cn	Gr	Total
WGCEP2002	7	3	24	17	17	9	9	–	6	15	15	5	4	2	38
±	3	2	3	4	4	2	2	–	2	3	3	3	2	1	4
Simple	1.9	2.6	19.6	16.7	15.6	7.2	7.1	0.0	10.0	17.1	16.2	9.0	8.8	−4.1	35.8
±	1.0	0.8	1.4	1.2	0.8	1.4	0.8	0.0	1.6	2.6	0.2	0.6	0.4	1.6	2.1
Preferred	2.4	3.0	20.2	17.1	16.4	6.6	6.5	4.0	6.2	12.9	12.7	7.0	6.7	5.4	37.8
±	1.0	0.8	1.4	1.4	1.0	2.4	1.4	3.0	0.8	0.6	0.4	1.8	1.4	0.6	4.5
Complex	4.9	5.1	20.6	16.0	13.0	7.8	7.6	3.6	4.2	12.4	20.6	6.9	6.5	6.2	38.9
±	1.2	0.8	1.4	1.8	3.8	2.4	1.4	3.2	1.0	1.8	2.2	1.8	1.4	0.6	4.6

[a]Fault system names from top row: SG, San Gregorio; SA, San Andreas; RC, Rodgers Creek; H, Hayward; C, Calaveras; GV, Green Valley; Gr, Greenville. Fault segments from second row: N, north; C, Central; S, south; Mr, Marin; SF, San Francisco; SCM, Santa Cruz Mountains; RC, Rodgers Creek; H, Hayward; WN, west Napa; Cn, Concord; Gr, Greenville. Total is the sum of SA-Mrn + RC + WN + GV. Rates in mm yr^{-1}, right lateral; 95% confidence bounds (±2σ). See Table ES3 for more model variations.

[39] In all cases except two, the best fitting shallow slip rate is less than the best fitting deep slip rate. Forcing the creep rate on the southern Calaveras fault to be equal to the deep slip rate increases the χ^2/DOF by an insignificant 0.4%, as there is little data coverage in this region. For the San Andreas fault south of San Juan Bautista (segment San Andreas-SJB), the calculated shallow slip rate of $\sim$20.3 mm yr^{-1} exceeds the deep strike-slip rate of $\sim$16.4 mm yr^{-1}. The higher slip rate is favored in models without a priori constraints and produces a 4% reduction in misfit compared to a model where the shallow and deep segments are required to slip at the same rate. I. A. Johanson and R. Bürgmann (Complexity at the junction of the Calaveras and San Andreas faults, submitted to *Journal of Geophysical Research*, 2004) show that slip in this area is spatially complex.

5. Dependence of Slip Rate on Model Parameters

5.1. Locking Depth

[40] The transition between creeping and locked behavior may not occur exactly at D_{95}, but we would expect the relative values of D_{95} to reflect the relative depth of this transition. To allow for the uncertainty in the absolute depth of the geodetic transition, we run the model multiple times and shift LD uniformly up and down over a range of depths. For example, D_{95} for the northern Hayward fault is 12 km and D_{95} for the Concord fault is 16 km. In our model runs, the LD of the Hayward fault is always 4 km shallower than the Concord fault, but we evaluate LD over the range of 3–17 km for the Hayward fault.

[41] We show model misfit as a function of LD in Figure 8. The best fit comes when the locking depths are about 5 km shallower than D_{95} for each segment. In model runs where faults are assigned a uniform LD, we find similar results. An 8 km uniform LD provides the best geodetic fit, even though it is also about 5 km shallower than the average 13 km D_{95} for the entire Bay Area. Locking depths based on D_{95} produce insignificantly better model fit than the best fitting uniform LD, but we prefer them because they are also consistent with the independent seismicity data set.

[42] Neither the uniform LD or deviations from D_{95} represent the absolute best statistical fit to the data. Both approaches shift all locking depths uniformly up or down. Since some of the largest differences between observed and model GPS velocities occur near the San Andreas fault in the southern Bay Area, Figure 8 is dominated by the preference for shallow slip in that area. For example, fixing LD of the Santa Cruz Mountains segment of the San Andreas fault to 5 km and keeping all other LD at D_{95} produces a better model fit than shifting the entire model shallower by 5 km (star, Figure 8; section 6.1). While simultaneously inverting for both LD and slip rate would avoid such sensitivity, *Prescott et al.* [2001] found that such joint inversions produce poorer constraints on the slip rate and result in less geologically reasonable slip distributions.

5.2. Shallow Creep Transition Depth

[43] Our treatment of shallow aseismic creep is oversimplified compared to faults in nature. Distributed slip models of the Calaveras and Hayward faults show a general pattern of high aseismic slip rates near the surface

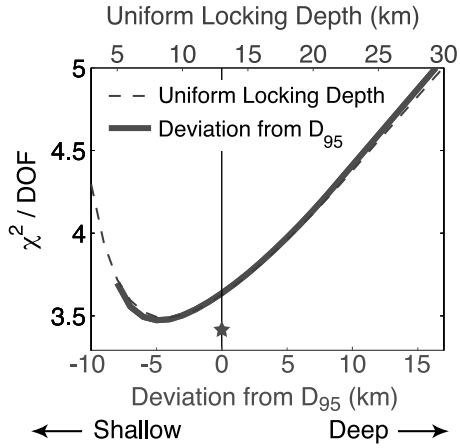

Figure 8. Model misfit versus locking depth for the Preferred model geometry. Uniform locking depth (thin dashed curve, top axis) assigns all dislocations the same LD. Deviation from D_{95} (thick solid curve, bottom axis) assumes that LD deviates by the amount indicated on the x axis deeper or shallower than D_{95} for their specific location. Negative values on the x axis are shallower than D_{95}. For faults with surface creep, the locking depth represents the transition between the deep slip rate and the shallow creep rate (LD = TD). The two curves are almost identical. Solid curve does not extend shallower than -8 because the shallowest locking depths would intersect the surface. Small star at $x = 0$ shows misfit for a model assuming LD = D_{95} everywhere except the Santa Cruz Mountains segment of SAF where we arbitrarily assign a very shallow LD of 5 km. This model gives better fit than uniform LD or deviations from D_{95}, highlighting the fact that the greatest misfit to GPS data occurs near that segment. See color version of this figure in the HTML.

with locked patches (very low aseismic slip rates) extending from a few kilometers depth to the seismic/aseismic transition (LD) [*Manaker et al.*, 2003; *Schmidt et al.*, 2005]. While the spatial resolution of our GPS data is not high enough to constrain the fine details of the aseismic slip distribution, we can explore the general distribution of slip within three depth intervals along creeping faults: (1) a shallow dislocation representing aseismic creep from the surface to some depth, TD; (2) a locked patch between the depths of TD and LD; and (3) a deep dislocation below LD. In the models considered thus far, we assumed that TD = LD, resulting in only two depth intervals along the fault (1 and 3 from above). Here we evaluate a variation on the Preferred model where TD is a fixed depth of 5 km on all creeping faults, representing shallow creep restricted to the upper 5 km (Model "Preferred, TD = 5"). The χ^2/DOF is 6% higher in "preferred, TD = 5" compared to the Preferred model. Slip rates for TD = 5 are almost all within the 95% confidence limits of the Preferred model, but there are some notable differences. The shallower TD produces less slip at intermediate depths, so slip rates on the remaining dislocations must be higher to yield the same surface deformation. The resulting shallow slip rate is universally faster than for cases where TD = LD. For creeping segments of the San Andreas and Calaveras faults, the shallower TD

produces slip rates 1–2 mm yr^{-1} faster than when TD = LD. By assuming TD = 5, the deep strike-slip rate on the central Calaveras fault increases from 12.9 to 15.0 mm yr^{-1} and the slip on the Hayward fault increases from 6.5 to 6.9 mm yr^{-1}. These slip increases are balanced by decreased slip on several other Bay Area faults such that the total slip across the entire Bay Area differs by <0.3 mm yr^{-1} as TD varies. We find similar results in a model where the shallow creep transition is exactly halfway between D_{95} and the surface (Model "Preferred, TD = $D_{95}/2$").

[44] This relative insensitivity to the shallow creep transition depth is similar to the findings of *Thatcher et al.* [1997] who describe a geodetic inversion of slip during the 1906 earthquake. They find that varying the depth extent of dislocations from 5 to 20 km causes <20% difference in the calculated slip on those elements. They also emphasize that even though the calculated slip is uniform along the entire dislocation, the inversion is more sensitive to the slip rate in the shallow portions of the fault that are closer to the surface geodetic data.

[45] We employ the assumption that TD = LD in our Preferred model because it produces the lowest χ^2/DOF. The improved fit may be due to the fact that slip rates between TD and LD are not exactly zero for the natural faults and that TD is likely to vary widely among the faults considered. By exploring a range of TD, we find that the shallow creep rates in our Preferred model are a lower bound, and the deep slip rates may vary from the Preferred model by 1–2 mm yr^{-1} for more complex distributions of shallow slip.

5.3. Fault-Normal Slip Rate Constraints

[46] The fault-normal slip rates from some previously published block models are sometimes of larger magnitude than geologically inferred slip rates [e.g., *McClusky et al.*, 2001; *Meade et al.*, 2002]. From our own modeling, we find this is especially true when faults are separated by horizontal distance less than a few locking depths and there is limited GPS data on the blocks. The inversion assigns high fault-normal slip rates of opposite signs to pairs of faults that are located close to one another. In such cases, the two slip rates balance one another so that the total fault-normal slip satisfies the far-field constraint. *Meade and Hager* [2005] refer to this phenomenon as "checker boarding." We found through trial and error that constraining the inversion to minimize the fault-perpendicular component on a very small number of segments reduces these slip rate oscillations throughout the entire model. We add an a priori constraint to the fault perpendicular slip rate on three segments whose strike is within 2.5° of the orientation of the PA-SNGV relative motion (northernmost Calaveras, northern Greenville, and northern Concord). We use a value of 0 ± 3 mm yr^{-1} for this constraint. These 1σ error bounds should allow convergence up to the total rate implied by previous geodetic studies for the entire Bay Area to occur on these three segments if the data actually require it. We apply an identical constraint to the Paicines fault because of its extremely close proximity to the much larger San Andreas fault. All other segments in the model are unconstrained. Adding these constraints increases the total χ^2 by only 0.5%. The constrained model does not cause a statistically significant change in any of the model estimates. Auxiliary material Figure ES1c shows that differences between our Preferred model (with the constraint) and an identical geometry without the constraint ("Preferred-Unclamped") are negligible. We feel that the model with these loose constraints produces physically reasonable slip rates without compromising the model fit or changing the qualitative interpretation of the results.

6. Discussion

6.1. Comparing the Models

[47] Figure 9 shows the residuals for the three main model geometries we discuss. The shading in Figure 9a shows the spatial distribution of the contribution to the total χ^2 misfit. Larger values (darker colors) indicate that the model is doing a particularly poor job of fitting the data in a certain area. The area around the epicenter of the 1989 Loma Prieta earthquake in the Santa Cruz Mountains has a systematic pattern in the residual velocities and a high total misfit. Northeast of this section of the San Andreas fault (SAF) the data could be fit by a higher right-lateral slip rate and <1 mm yr^{-1} of fault perpendicular motion. Such an observation might indicate that accelerated postseismic deformation along the fault persists at rates of ~1 mm yr^{-1} more than a decade after the 1989 earthquake. Stations near San Juan Bautista, also along the SAF, are fit poorly, though the orientations of residual velocities are not entirely systematic. Together, the two areas along the SAF in the southern Bay Area and a few strong outliers dominate the χ^2 statistics. Models that improve the fit of those regions may have lower total χ^2 even if they result in a worse fit throughout the rest of the model.

[48] The shading in Figures 9b and 9c and ES1 show where the weighted residuals (χ^2) for each model differ from the Preferred model. We calculate χ^2 for the two components of each GPS velocity in each model and then subtract this from χ^2 in the Preferred model. Note how changes to the geometry of the model in one location can alter the predicted velocity throughout the model.

[49] The Simple model (Figure 9b) does a poor job fitting sites east of the Calaveras and San Andreas faults in the southern Bay Area. Figure 3 illustrates that the fit to sites on the SNGV block is also poorer in the Simple model, with a systematic rotation of the predicted velocities to the east (clockwise) of the data. The slip rate on the Mount Lewis Trend and Greenville faults is left lateral for the Simple model, which is the opposite sense from earthquake focal mechanisms in the region [e.g., *Kilb and Rubin*, 2002]. The systematic misfit of GPS data and the opposite sense of slip are the motivation for including a "Valley Margin deformation zone" in our Preferred model. *Unruh and Sawyer* [1998] suggest that the Greenville fault connects with the Ortigalita fault, a Holocene active fault with both vertical and strike-slip components that parallels the San Andreas fault system along the eastern margin of the Coast Ranges [*Bryant and Cluett*, 2000]. We extend a vertical fault through the trace of the Ortigalita fault, connecting to the San Andreas at the Carrizo Plain in the south and to the Greenville fault in the north. Geologic and geophysical evidence supports the existence a major fault structure in

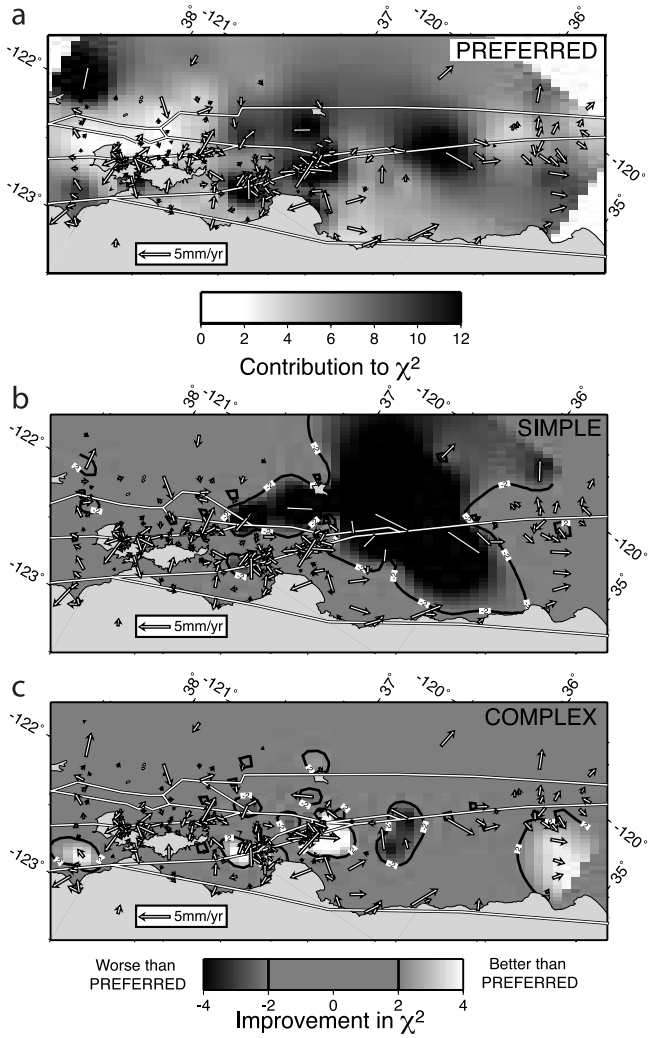

Figure 9. Residual velocity (difference between data and model) for three different model geometries. (a) Relative contribution (shading) to the χ^2 misfit statistic of each station in our Preferred model. Dark colors indicate that the model does a poor job of fitting the data within the error bounds. (b) and (c) Differences between the given model and the Preferred model (highlighted by color scale). Values of $|\chi^2| \leq 1$ for each data parameter indicate that the residual velocity is the same magnitude as the 1σ uncertainty. Contour lines at ±2. See color version of this figure in the HTML.

this vicinity along the eastern front of the Coast Ranges [e.g., *Wong and Ely*, 1983; *Wentworth and Zoback*, 1989; *Fuis and Mooney*, 1990]. Seismicity, including the 1983 Coalinga event [*Wong and Ely*, 1983] suggest that a broad zone of faults may actually be accommodating the total relative motion across the Coast Ranges, and not a single discrete structure. Because the GPS data are sparse in this region, we are not able to differentiate between a single fault structure and a zone of faults along the eastern Coast Ranges, nor are we sensitive to the dip of the structure or structures.

[50] The Complex model (Figure 9c) provides strong improvement to the model fit (8% reduction in total χ^2/DOF), particularly the areas most poorly fit in the Preferred model near Loma Prieta and San Juan Bautista. The Complex model has three blocks (Pleasanton, Sargent, and Paicines) added to the Preferred model's 8 blocks. The Paicines block only has a single GPS station on it and is therefore poorly constrained by the data. Improved fit to data around San Juan Bautista accounts for the greatest reduction in misfit, probably because we add two additional blocks (Sargent and Paicines) in this area (and therefore additional model parameters). Even though this model has the lowest misfit, the sparse data coverage on these blocks and the known complexity of slip in this area suggest that the Complex model may not be the most accurate block model representation of the fault system in the southern Bay Area.

6.2. Comparison With Geologically Determined Slip Rates

[51] Numerous geologic investigations have determined long-term average slip rates for Bay Area faults during portions of the Holocene. Such studies provide essential input into earthquake hazard assessment and a comprehensive summary of previous work has been compiled for this purpose ("WGCEP2002"[*Working Group on Northern California Earthquake Probabilities*, 2003, Chapter 3]). In general, the geodetically observed slip rates agree well with the values from WGCEP2002 (Tables 4 and ES4). Slight differences could reflect a combination of errors in each data set or a real difference in the behavior of faults during the last decade compared to the last several thousand years. Both the Greenville fault and the Green Valley/Concord fault system have slip rates higher than preferred bounds from WGCEP2002. More recent paleoseismological work by *Sawyer and Unruh* [2002] constrains the slip rate on the Greenville fault to 4.1 ± 1.8 mm yr^{-1}. This estimate agrees with the slip rate from our Preferred model (5.4 ± 0.6 mm yr^{-1}) within the error bounds of each rate. The northern San Gregorio fault has a slip rate lower than the geologic bounds. In our model, all slip from the San Gregorio transfers to the Marin segment of the San Andreas fault, which also has a slip rate lower than the geologic bounds. The Hayward fault, Calaveras fault, and San Andreas fault from the Peninsula south all have slip rates within the bounds described by WGCEP2002, but slightly lower than the most probable value. Most notably, none of our model variations produce slip rates on the Hayward fault as high as the WGCEP2002 estimate. WGCEP2002 does not explicitly consider the effects of the West Napa fault as a possible extension of the Calaveras fault, while we find a slip rate of ~3.5 mm yr^{-1}. We find a strike-slip rate for the Valley Margin deformation zone of 5.4 ± 1.0 mm yr^{-1} in our Preferred model. WGCEP2002 does not estimate a slip rate for this region, but geologic investigations by *Anderson and Piety* [2001] show that the northern Ortigalita fault carries 0.5–2.5 mm yr^{-1} of slip. The slip rate across the entire eastern Coast Ranges must be at least as high as the rate for this single structure.

[52] A forward model of the WGCEP2002 fault parameters (long-term slip, fault width, and shallow locking ratio, R; "Preferred-WG02") has χ^2/DOF of 6.8, indicating that the slip rates from our Preferred model

provide a substantially better fit to the BĀVŪ geodetic data.

6.3. Fault Connections: Northern Calaveras

[53] Faults that are connected can transfer slip between one another and potentially rupture together in large earthquakes. Such connections can be complex and often are not mapped, but we must make inferences about how faults connect to define block boundaries. While these inferences add nonuniqueness to our models, this feature of block modeling also allows us to test various scenarios of fault connections to see if they are consistent with our observed surface deformation rates.

[54] The northern termination of the mapped Calaveras fault is an area where there is still significant debate about which faults are connected to each other and where slip on the Calaveras gets transferred after the mapped trace terminates. *Galehouse and Lienkaemper* [2003] note that the nearly identical surface creep rates on the two systems imply that the Calaveras connects eastward to the Concord-Green Valley fault via a mechanically favorable releasing step. Others [*Unruh and Lettis*, 1998; *Unruh et al.*, 2002] suggest that fold and fault geometry in the East Bay Hills indicate that the Calaveras steps westward with a restraining geometry, connecting to the West Napa fault and eventually transferring slip to the Rodgers Creek fault somewhere north of San Pablo Bay. Determining how slip is distributed between faults in the northern East Bay has important implications for the seismic hazard in these growing suburban areas. Using our block model, we focus on this junction and test a wide range of model geometries.

[55] Overall, there is no substantive difference in model fit between models where the Calaveras steps east versus west, though there are some scenarios where the east stepping model produces a slightly smaller model misfit. Here we describe the effects of the two models "CalaverasWest" and "CalaverasEast," which are both based on the Preferred model.

[56] Forcing the Calaveras to transfer all slip to the west (CalaverasWest) brings slip on the Calaveras system geographically closer to the Hayward/Rodgers Creek system. The deformation gradient in the GPS data near these two fault systems limits the combined slip that can be accommodated by locked faults. When the two fault systems are close together, there is a tradeoff where more slip on the Calaveras/West Napa system requires less slip on the Hayward/Rodgers Creek system. Slip on the Hayward fault in the CalaverasWest model is 5.2 mm yr^{-1}, well below the $\sim$9 mm yr^{-1} geologic slip rate estimated from offset stream channels. The χ^2/DOF for CalaverasWest is 2.0% higher than the Preferred model, but CalaverasWest affects the fit to stations as far away as Parkfield (Figure ES1a).

[57] CalaverasEast produces a higher slip rate on the Hayward fault of about 7.5 mm yr^{-1}, but also allows for 10.0 mm yr^{-1} on the Green Valley fault because the Green Valley fault carries the combined slip from both the northern Calaveras fault and the Valley Margin deformation zone. The χ^2/DOF of the CalaverasEast model is 0.8% higher than the Preferred model and only affects the fit to GPS data in the northern Bay Area near where the model geometry differs.

[58] Our Preferred model allows Calaveras slip to transfer both east and west. In it, slip rates are about halfway between the two scenarios CalaverasWest and CalaverasEast. Other model geometries that include the Mount Lewis trend, exclude the Valley Margin deformation zone, or use slightly different fault geometries have similar results.

[59] Despite the fact that there are a number of GPS stations in the area of interest, it may never be possible to distinguish between these different scenarios using geodetic data alone. The West Napa and Green Valley faults are located <10 km apart, similar to the geodetic locking depth. It is difficult to distinguish between two elastic dislocations buried about 15 km below the surface and spaced only 10 km apart. The added constraint from block offset could help distinguish between the two faults, especially as the details of shallow creep on the Green Valley fault are determined more precisely.

6.4. Dipping Faults

[60] All fault segments in our model are vertical, and in this section we discuss the technical and conceptual limitations to using dipping faults in a block model based on dislocation theory.

[61] For vertical faults throughout all our models, we allow for the faults to open or the blocks to converge as a proxy for dip-slip faulting. This "tensile-slip" component (auxiliary material Table ES6) accurately represents the total block motion, but the symmetric strain accumulation about a vertical fault is not a perfect analog for dipping faults. The differences between dip slip and tensile slip are pronounced for vertical deformation, but the differences are minor when only modeling horizontal components of GPS velocity.

[62] Because thrust faulting may be important locally in the eastern Bay Area, we explore a variation on the Preferred model that includes dipping Mount Diablo and Mount Oso thrust faults ("Preferred-Thrust"). The χ^2/DOF for "Preferred-Thrust" is just 0.2% higher than the Preferred model and all slip rates are within 0.2 mm yr^{-1} of the Preferred model.

[63] All of our model geometries produce convergence across the Mount Diablo fault. Variations on the Simple and Complex models that include a dipping Mount Diablo fault find it has a reverse slip of 2.7 and 5.7 mm yr^{-1}, respectively. In the "Preferred-Thrust" model, we find 3.9 $\pm$ 1.0 mm yr^{-1} of reverse slip along with 4.0 $\pm$ 0.2 mm yr^{-1} of strike slip across the fault. The reverse component is within the 1.3–7.0 mm yr^{-1} range determined from restorations of geologic cross sections [*Unruh and Sawyer*, 1997]. The ratio between strike-slip and horizontal shortening components depends on fault strike, but the total magnitude of the slip vector does not. The dip-slip magnitude is particularly sensitive to fault dip because horizontal shortening is projected onto the dipping fault. We use a dip of 38°N for the Mount Diablo thrust, based on the 30–45° range in WGCEP2002. Because of the Mount Diablo thrust system's role of transferring slip from the Greenville fault to the Concord/Green Valley system in our model, it must carry several millimeters per year of slip consistent with block motion. A substantial portion of this slip must be strike-slip deformation because the thrust system's average strike is not perfectly

perpendicular to the relative block motion that it must accommodate.

6.5. Convergence in the Coast Ranges

[64] Perfect transform faulting can occur when the rotation axes for a sequence of blocks are located at the same point but have different rates. Faulting will only be pure strike slip everywhere if all of the block boundaries are parallel to the small circle path of the relative motion vector and parallel to one another (so that they never intersect). The situation in the Bay Area meets neither of these conditions perfectly: the rotation axes of Bay Area blocks follow a systematic progression between the NA-PA and NA-SNGV blocks, and the faults in the system are rarely parallel to one another. Abundant folds and thrust faults roughly parallel to the San Andreas system suggest that pure strike-slip motion on the major Bay Area faults does not accommodate all of the plate boundary motion. We use our block model to constrain the magnitude and location of any fault-perpendicular convergence.

[65] *Savage et al.* [1998] and *Savage et al.* [2004] determine the regional strain field in the Bay Area. They find that the Bay Area as a whole undergoes an insignificant amount of areal dilatation. They identify localized zones where contraction would give rise to thrust faulting such as the region around the 1989 Loma Prieta rupture.

[66] In contrast, some authors suggest that Bay Area GPS data require a small component of fault-normal contraction between the SNGV block and the Bay Area. *Prescott et al.* [2001] analyze a profile between Point Reyes and Davis and find $\sim$3.8 $\pm$ 1.5 mm yr^{-1} of shortening over a 25-km-wide zone localized at the margin of the Great Valley. For a similar time span and data covering a larger range of latitudes in the Bay Area, *Murray and Segall* [2001] find $\sim$2.4 $\pm$ 0.4 mm yr^{-1} of contraction accommodated over a similarly narrow (<15 km) zone. *Freymueller et al.* [1999] present data from further north and conclude that shortening must be <1–3 mm yr^{-1}. *Pollitz and Nyst* [2005] fit regional GPS data with a viscoelastic model and find 3 mm yr^{-1} of shortening perpendicular to a model boundary oriented N34°W. Additional campaign GPS observations since the publication of those papers reduced the scatter in the data. Here we discuss new constraints on the magnitude of convergence in the Bay Area and the area over which it is accommodated.

[67] Several of the previous observations of convergence in the Coast Ranges were based on the presentation and interpretations of profiles across the plate boundary, such as we show for BĀVŪ in Figure 10 [e.g., *Murray and Segall*, 2001, Figure 2; *Prescott et al.*, 2001, Figure 5; *Savage et al.*, 2004, Figure 4]. These plots show the two horizontal components of GPS velocity projected onto a coordinate system with axes parallel and perpendicular to an "average" plate boundary orientation (usually parallel to the PA-NA relative motion and not PA-SNGV). The shape of the profile is highly dependent on the choice of the orientation used to define this average. Because the deformation field is projected onto a single orientation, pure strike-slip motion on faults with a range of orientations can yield an apparent "fault normal contraction" signal. Figure 11 shows GPS data from the North Bay profile perpendicular to the San Andreas fault (N33.85°W, Figure 11a) and the azimuth of maximum shear strain from *Savage et al.* [2004] (N30°W, Figure 11b). When accounting for the formal uncertainties, both profiles are statistically permissive of a scenario with no net convergence. The systematic pattern in both plots, however, implies that the variations are not random scatter. In the top profile, there is an abrupt step in the data at the Green Valley fault, suggesting $\sim$2 mm yr^{-1} of contraction between the Pacific and SNGV accommodated near that structure. In the latter example, there is no net plate boundary normal motion between the Pacific and SNGV blocks (the data have nearly the same value on both ends of the profile). These two different projections of the same data yield different conclusions about the magnitude and location of convergence in the Bay Area, even though the profile orientation differs by only 4°. This comparison should emphasize the hazard of representing spatially complex two-dimensional (2-D) velocity data in an essentially 1-D illustration. The localized signal of contraction previously interpreted in the Coast Ranges using these profiles is likely strike-slip motion of the Green Valley fault whose orientation differs prominently from the average plate boundary. Evidence for convergence cannot come from these "plate boundary perpendicular" profiles.

[68] More precise and rigorous measurements of the convergence across individual Bay Area faults comes from comparing the orientation of vectors representing the relative motion between blocks (calculated in our model) and the orientation of individual mapped faults accommodating that motion [e.g., *Argus and Gordon*, 2001]. The vectors in Figure 12 show the orientation and magnitude of relative motion that is accommodated by faults in our Preferred model assuming that the northeastern side of each fault is fixed. The relative motion is, in general, nearly parallel to local fault strike. Resolving these vectors onto the local fault orientation indicates the precise convergence that must be accommodated. These results are reported as "tensile slip rates" in Table ES6. The bend in the San Andreas fault at the Santa Cruz Mountains shows as much as 4.9 $\pm$ 0.6 mm yr^{-1} of contraction perpendicular to the segment (likely accommodated by a number of thrust faults alongside the San Andreas fault). In general, motions east of the bay are slightly clockwise of the faults, indicating convergence across the block boundaries, which is balanced by a slight extensional component west of the bay. The magnitude of convergence increases from 0.1 $\pm$ 1.0 mm yr^{-1} along the northern Hayward fault to 1.1 $\pm$ 1.0 mm yr^{-1} on the southernmost segment of the Hayward fault (Hayward_4). The segment connecting the Hayward and Calaveras faults that roughly parallels the seismicity beneath Mission Peak (Hayward_South) has 3.0 $\pm$ 1.0 mm yr^{-1} of convergence. Along the eastern margin of the Coast Ranges, the Valley Margin deformation zone converges by 2.7 $\pm$ 0.8 mm yr^{-1}. The Concord/Green Valley system requires a similar magnitude of convergence, but is located so close to the west Napa fault that the elastic model would probably not be able to distinguish between deep tensile slip on the two faults (e.g., section 5.3). We therefore treat the Concord/Green Valley and west Napa fault systems together and find a statistically insignificant 1.9 $\pm$ 3.0 mm yr^{-1} of convergence. The San Gregorio fault and Marin segment of the San Andreas fault both show minor extension, with 2.9 $\pm$ 0.6

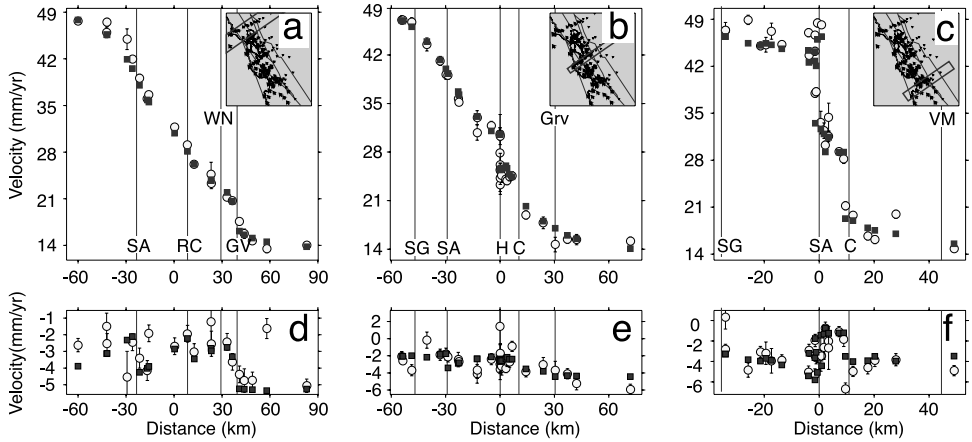

Figure 10. Profiles of GPS velocities along transects perpendicular to the San Andreas fault system. (top) Component of the velocity parallel to N33.85°W, the approximate strike of the San Andreas fault in the Bay Area. (bottom) Component of velocity perpendicular to N33.85°W. Circles are observations with 1σ uncertainties. Squares are model fit from our Preferred model. For each profile, we include velocities within the box shown in the inset map. See color version of this figure in the HTML.

and 1.9 ± 0.6 mm yr^{-1}, respectively. It is not possible to determine if this motion is accommodated onshore or offshore because of the sparse data west of these faults. Either way, this slight extension is required to satisfy the total PA-SNGV relative motion. We therefore agree with the assertion by *Savage et al.* [2004] that while there are localized zones of convergence related to fault geometry, the geodetic data do not show evidence of measurable net convergence across the Bay Area.

6.6. Implications for Fault System Development

[69] What does the systematic progression of poles of rotation from west to east shown in Figure 6 tell us about the evolution and behavior of the Bay Area faults? There are two possibilities: (1) the rotation axes reflect the existing geometry of the faults, and blocks merely move in a manner that is kinematically and mechanically favorable, given the orientation of preexisting weaknesses in the area; or (2) active faults are oriented at an optimal angle to the far-field motion of the plates that drive them (to produce pure strike-slip faulting, for example) [*Wesnousky*, 1999]. Faults that are less optimally oriented might be abandoned over time. Distinguishing the relative contributions of these two end-member processes is beyond the scope of this work, but we can discuss the latter option. Some faults in the Bay Area such as the San Andreas are oriented parallel with present day PA-NA motion, despite the fact that the plate boundary that should exert a controlling influence on the Bay Area is between the Pacific and SNGV blocks [e.g., *Argus and Gordon*, 2001; W. Lettis, personal communication, 2004]. The orientation of these faults could be inherited from a time when the SNGV block moved more closely with North America. Figure 12a shows the geometry of the San Andreas fault system compared with small circle traces parallel to the relative motion of the PA-NA and PA-SNGV. Faults parallel to the PA-SNGV relative motion show up as horizontal lines in this map projection. Few, if any, of the faults in the Bay Area are horizontal over much of their extent. Most notably, almost the entire San

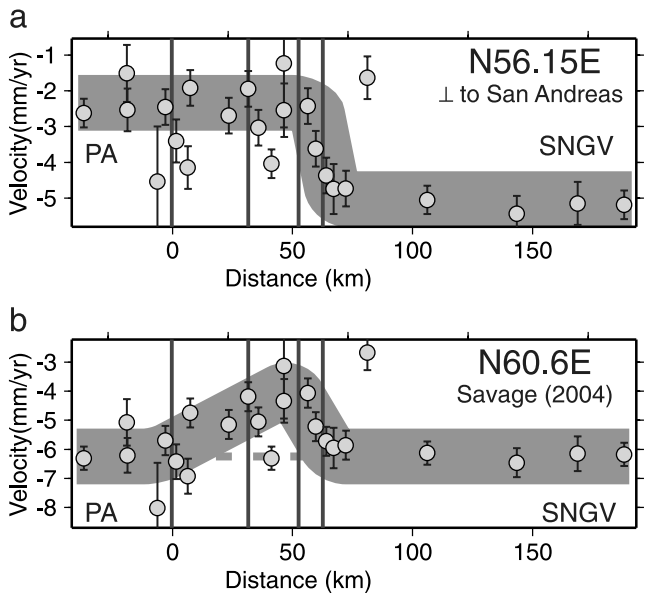

Figure 11. Effect of profile orientation on conclusions about convergence. (a) Same as Figure 10d showing the profile-perpendicular component of velocities from the northern Bay Area along a profile at N56.15°E, perpendicular to the strike of the San Andreas fault. (b) Exact same velocities as Figure 11a projected onto a slightly different orientation profile, N60.6°E (the orientation of maximum extension from *Savage et al.* [2004]). The orientation perpendicular to PA-SNGV motion at this latitude from our Preferred model is N59.6°E. Thick gray bands show possible interpretations of the data. Dashed line in Figure 11b is horizontal for reference. Even though profiles differ by only 4°, the apparent convergence between the Pacific and SNGV blocks changes dramatically. (Figure was inspired by comments of J. Savage, 2004). See color version of this figure in the HTML.

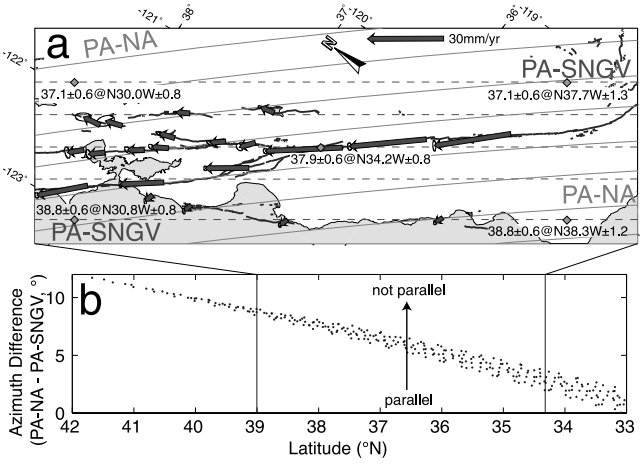

Figure 12. (a) Calculated orientation of relative motion for PA-NA (light colored, solid curves) and PA-SNGV (dashed horizontal lines) based on rotation axes from our Preferred model. Map is projected about the PA-SNGV pole so that fault segments and velocities parallel to the PA-SNGV relative motion show up as horizontal. Velocity vectors with error ellipses are the relative motion vector accommodated by each fault at the given location, assuming that the northeastern side of the fault (top of figure) is held fixed. Vectors parallel to fault indicate pure strike-slip motion. Because the eastern block is fixed on these dominantly right-lateral faults, vectors with azimuths clockwise of their respective fault segment indicate convergence and vectors trending counterclockwise represent divergence. In general, note that faults nearer to the top of the figure tend to show more convergence, while those near the bottom of the figure show a slight divergence. Solid diamonds with labels are PA-SNGV rate in mm yr^{-1} and azimuth at select locations. (b) Difference in azimuth between the PA-NA and PA-SNGV relative motion vectors for points on a regular grid spaced from the area of the map above and extensions farther north and south. The two differ in azimuth by only 2° at the south end of the map and almost 8° at the north end. Note that this graph extends farther north and south beyond the Great Valley to accentuate the trend of the line and shows that the two relative velocities become parallel just south of the Great Valley. The parallel motions would theoretically allow pure transform faulting to accommodate all of the relative motion across southern California if the Great Valley extended south to a latitude of 33°N. Vertical lines indicate the extent of Figure 11a. See color version of this figure in the HTML.

Andreas fault is rotated counterclockwise by ~5° from the ideal PA-SNGV motion (with the Santa Cruz Mountains segment rotated >20° away). It is, in fact, roughly parallel with the predicted PA-NA motion from our Preferred model. The central Calaveras, central Greenville, Concord, and Ortigalita faults have strikes approximately parallel to PA-SNGV motion. Other fault segments, such as the southern Calaveras, the Green Valley, and San Gregorio faults strike as much as 10° clockwise of the present PA-SNGV motion. With the exception of the San Gregorio fault, faults striking parallel to or clockwise of PA-SNGV motion are east of the bay. The general disagreement between fault strike and total plate boundary motion suggests that present-day plate motion cannot explain the orientation of active faults in the Bay Area. *Wakabayashi* [1999] shows a general progression where the oldest active faults in the Bay Area initiated in the west while the youngest faults in the Bay Area are to the east (though he emphasizes that there are abundant exceptions to this trend, especially for faults that appear to have been abandoned and are currently inactive that show a much more complex age distribution). We focus here on the active faults because those are the ones that are relevant for rotation axes derived from active deformation measurements. Figure 13 explores the relationship between the orientation of plate motion in the past and the timing of initiation for individual fault segments. We calculate the PA-SNGV motion by subtracting the Basin and Range motion (reference point A) [*Wernicke and Snow*, 1998] from PA-NA motion [*Atwater and Stock*, 1998]. The exact timing of initiation for many of the faults is not constrained reliably enough to make any definitive conclusions from Figure 13. However, the plate reconstructions emphasize that the relative motion between PA-SNGV has rotated by >30° during the lifetime of many Bay Area faults, and that this range encompasses most of the range of fault strikes observed in the Bay Area. In light of these dramatic changes in plate motion in the past, it is probably unwise to make conclusions about fault system development from our present-day GPS-derived rotation axes.

7. Conclusions

[70] The interseismic velocities at over 200 Bay Area stations provide a comprehensive picture of crustal deformation in the region. The block modeling approach enables us to interpret these velocities at a wide range of spatial scales.

[71] We constrain the motion of blocks in the Bay Area relative to adjacent global plates (NA and PA), as well as the SNGV microplate. Individual blocks within the Bay Area do not move about identical poles of rotation of any of these major blocks as a "perfect transform" system, but instead have poles at intermediate locations that vary in a systematic pattern from east to west across the Bay Area (Figure 6). This pattern may have implications for the development of the fault system.

[72] Looking at the Bay Area region, we quantify the slip rates of individual faults. We use precise relocations of earthquakes to determine the maximum depth of seismicity as a proxy for the local seismic/aseismic transition. We find slip rates that are typically within the uncertainty of geologic estimates (Table 4). We also document substantial slip on segments that have not been emphasized in previous studies. Models that include up to 4 mm yr^{-1} of strike slip on the West Napa fault north of San Pablo Bay provide almost identical model fits to those that exclude this fault. In our Preferred model, we favor this geometry because it is consistent with geologic evidence showing that some slip from the Calaveras fault is transferred westward, eventually connecting to the West Napa fault system. Adding a fault along the eastern margin of the Coast Ranges in our Preferred model produces lower misfit and a geologically reasonable slip sense (right lateral) on the Greenville fault. This fault, running parallel to the San Andreas through

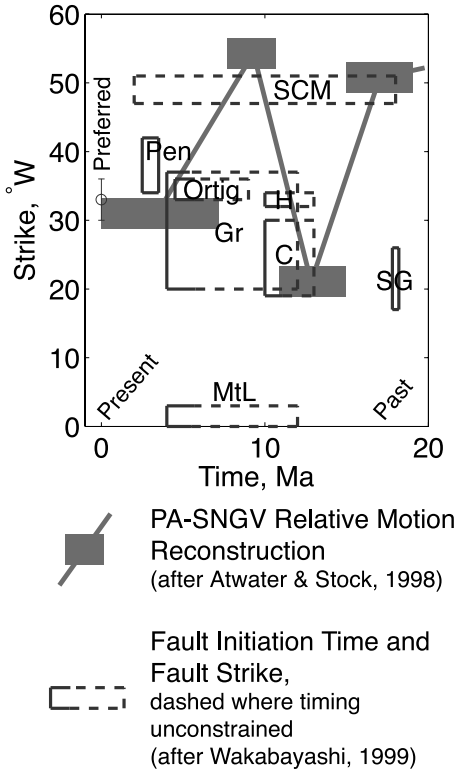

Figure 13. Comparison of the present-day strike of Bay Area faults (open rectangles) with the orientation of relative motion between the Pacific and SNGV blocks (solid rectangles and line connecting them). Fault abbreviations are C, Calaveras; Gr, Greenville; H, Hayward; MtL, Mt, Lewis; Ortig, Ortigalita; Pen, Peninsula segment of SAF; SCM, Santa Cruz Mountains segment of SAF; SG, San Gregorio. Fault initiation times come from *Wakabayashi* [1999] and are dashed where loosely constrained. For example, the San Gregorio fault's initiation is well constrained, but the Mount Lewis fault could have initiated as early as 12 Ma (dashed right edge of box) and must have initiated by 5 Ma (solid left edge of box). Height of open box represents range of fault strikes for the given fault. Relative motion is reconstructed in the geologic past by *Atwater and Stock* [1998] (PA-NA) and *Wernicke and Snow* [1998] (SNGV-NA). They report average rates over the given time interval indicated by the width of the solid bars. The height is arbitrary because no uncertainty is reported. Circle with error bars at present-day shows relative motion calculated from our Preferred model. See color version of this figure in the HTML.

central California carries as much as 5 mm yr^{-1} of right-lateral slip. Poor data coverage near the model fault segment prevent us from determining if the deformation is accommodated by a single structure or a broad zone with many structures as might be implied by the distribution of moderate thrust earthquakes within the Diablo and Coast Ranges. While such events imply a substantial component of fault-normal convergence in the region, the BĀVŪ geodetic data are fit best with negligible convergence across the Coast Ranges. Our block modeling approach provides one of the first geodetic constraints on the slip rates of several other faults because we include global GPS data from the Pacific plate and the physical constraint of coherent block motion. These faults include the San Gregorio fault (2.4 ± 0.5 mm yr^{-1} right-lateral slip rate) and the Mount Diablo thrust (3.9 ± 0.5 mm yr^{-1} reverse slip and an almost equal magnitude of right-lateral strike slip). Overall, we find that the slip rates we determine fit GPS data substantially better than the slip rates defined in WGCEP2002.

[73] We explore the possibility that the northern Calaveras fault transfers its slip east to the Concord/Green Valley fault, west to the West Napa fault system, or a combination of the two. The data slightly favor the eastern step over the western step alone, but we prefer models where both connections are included because they most closely reproduce the geologically inferred slip rate on the Green Valley fault and the lowest total model misfit.

[74] In block modeling, three-dimensional fault geometry and connectivity have a very strong impact on the interpretation of surface deformation. While we systematically explored an extremely wide range of model geometries in this work, we look forward to further geologic constraints on fault geometry in three dimensions to improve the reliability of block models. The ability to iteratively explore these different block geometries and test their consistency with geodetic data make the block modeling approach an excellent tool for understanding fault kinematics in the Bay Area.

[75] **Acknowledgments.** Dozens of students at the University of California, Berkeley, generously volunteered their time to help collect high-quality geodetic data throughout the Bay Area. This material is based on work supported by USGS NEHRP external grant 04-HQGR-0119 and a National Science Foundation Graduate Research Fellowship. Continuous data from the BARD network and campaign GPS data collected by the U.S. Geological Survey were obtained from the Northern California Earthquake Data Center. We acknowledge SOPAC at University of California, San Diego, for easy access to GAMIT processing results of global and regional networks. J. Beavan, Y. Bock, and J. Savage provided useful reviews of the manuscript. Robert King provided suggestions on GPS error scaling methodology. Jeff Unruh helped us define the most realistic model geometry possible. We are grateful to Brendan Meade for providing us his well-documented block modeling code. Berkeley Seismological Laboratory contribution 05-04.

References

Altamimi, Z., P. Sillard, and C. Boucher (2002), ITRF2000: A new release of the International Terrestrial Reference Frame for earth science applications, *J. Geophys. Res.*, *107*(B10), 2214, doi:10.1029/2001JB000561.

Anderson, L. W., and L. A. Piety (2001), Geologic seismic source characterization of the San Luis-O'Neill area, eastern Diablo Range, California, *Seismotectonic Rep. 2001-2*, U.S. Bur. of Reclamation, Denver, Colo.

Argus, D. F., and R. G. Gordon (1991), Current Sierra-Nevada North America motion from very long base-line interferometry—Implications for the kinematics of the western United States, *Geology*, *19*, 1085–1088.

Argus, D. F., and R. G. Gordon (2001), Present tectonic motion across the Coast Ranges and San Andreas fault system in central California, *Geol. Soc. Am. Bull.*, *113*(12), 1580–1592.

Atwater, T., and J. Stock (1998), Pacific-North America plate tectonics of the Neogene southwestern United States: An update, *Int. Geol. Rev.*, *40*(5), 375–402.

Bennett, R. A., W. Rodi, and R. E. Reilinger (1996), Global positioning system constraints on fault slip rates in southern California and northern Baja, Mexico, *J. Geophys. Res.*, *101*(B10), 21,943–21,960.

Bennett, R. A., B. P. Wernicke, N. A. Niemi, A. M. Friedrich, and J. L. Davis (2003), Contemporary strain rates in the northern Basin and Range province from GPS data, *Tectonics*, *22*(2), 1008, doi:10.1029/2001TC001355.

Blanpied, M. L., D. A. Lockner, and J. D. Byerlee (1995), Frictional slip of granite at hydrothermal conditions, *J. Geophys. Res.*, *100*(B7), 13,045–13,064.

Bryant, W., and S. Cluett (2000), Fault number 52b, Ortigalita fault zone, Los Banos Valley section, in *Quaternary Fault and Fold Database of the United States*, version 1.0, *U.S. Geol. Surv. Open File Rep.*, *03-417*. (available at http://qfaults.cr.usgs.gov)

Bürgmann, R., D. Schmidt, R. M. Nadeau, M. A. d'Alessio, E. Fielding, T. V. McEvilly, and M. H. Murray (2000), Earthquake potential along the northern Hayward fault, California, *Science*, *289*, 1178–1182.

Cox, A., and R. B. Hart (1986), *Plate Tectonics: How it Works*, Blackwell Sci., Malden, Mass.

Freymueller, J. T., M. H. Murray, P. Segall, and D. Castillo (1999), Kinematics of the Pacific-North America plate boundary zone, northern California, *J. Geophys. Res.*, *104*(B4), 7419–7441.

Fuis, G. S., and W. D. Mooney (1990), Lithospheric structure and tectonics from seismic refraction and other data, in *The San Andreas Fault System, California*, edited by R. E. Wallace, *U.S. Geol. Surv. Prof. Pap.*, *1515*, 207–236.

Galehouse, J. S., and J. J. Lienkaemper (2003), Inferences drawn from two decades of alinement array measurements of creep on faults in the San Francisco Bay Region, *Bull. Seismol. Soc. Am.*, *93*(6), 2415–2433.

Herring, T. A. (2002), GLOBK, global Kalman filter VLBI and GPS analysis program, version 10.1, Mass. Inst. of Technol., Cambridge, Mass. (Available at http://www-gpsg.mit.edu/simon/gtgk/index.htm)

Kilb, D., and A. M. Rubin (2002), Implications of diverse fault orientations imaged in relocated aftershocksof the Mount Lewis, M_L5.7, California, earthquake, *J. Geophys. Res.*, *107*(B11), 2294, doi:10.1029/2001JB000149.

King, R. W., and Y. Bock (2002), Documentation for the GAMIT GPS analysis software, version 10.0,, Mass. Inst. of Technol., Cambridge.

Lachenbruch, A. H., and J. H. Sass (1980), Heat flow and energetics of the San Andreas fault zone, *J. Geophys. Res.*, *85*(B11), 6185–6222.

Lienkaemper, J. J., J. S. Galehouse, and R. W. Simpson (2001), Long-term monitoring of creep rate along the Hayward fault and evidence for a lasting creep response to 1989 Loma Prieta earthquake, *Geophys. Res. Lett.*, *28*(11), 2265–2268.

Magistrale, H. (2002), Relative contributions of crustal temperature and composition to controlling the depth of earthquakes in southern California, *Geophys. Res. Lett.*, *29*(10), 1447, doi:10.1029/2001GL014375.

Manaker, D. M., R. Brgmann, W. H. Prescott, and J. Langbein (2003), Distribution of interseismic slip rates and the potential for significant earthquakes on the Calaveras fault, central California, *J. Geophys. Res.*, *108*(B6), 2287, doi:10.1029/2002JB001749.

McCaffrey, R. (2002), Crustal block rotations and plate coupling, in *Plate Boundary Zones*, *Geodyn. Ser.*, vol. 30, edited by S. Stein and J. T. Freymueller, pp. 101–122, AGU, Washington.

McClusky, S. C., S. C. Bjornstad, B. H. Hager, R. W. King, B. J. Meade, M. M. Miller, F. C. Monastero, and B. J. Souter (2001), Present day kinematics of the Eastern California Shear Zone from a geodetically constrained block model, *Geophys. Res. Lett.*, *28*(17), 3369–3372.

Meade, B. J., and B. H. Hager (2005), Block models of crustal motion in southern California constrained by GPS measurements, *J. Geophys. Res.*, *110*, B03403, doi:10.1029/2004JB003209.

Meade, B. J., B. H. Hager, S. McClusky, R. E. Reilinger, S. Ergintav, O. Lenk, A. Barka, and H. Ozener (2002), Estimates of seismic potential in the Marmara Sea region from block models of secular deformation constrained by Global Positioning System measurements, *Bull. Seism. Soc. Am.*, *92*, 208–215.

Murray, M. H., and P. Segall (2001), Modeling broadscale deformation in northern California and Nevada from plate motions and elastic strain accumulation, *Geophys. Res. Lett.*, *28*(22), 4315–4318.

Okada, Y. (1985), Surface deformation due to shear and tensile faults in a half-space, *Bull. Seismol. Soc. Am.*, *75*(4), 1135–1154.

Pollitz, F. F., and M. C. J. Nyst (2005), A physical model for strain accumulation in the San Francisco Bay region, *Geophys. J. Int.*, *160*, 302–317.

Prescott, W. H., J. C. Savage, J. L. Svarc, and D. Manaker (2001), Deformation across the Pacific-North America plate boundary near San Francisco, California, *J. Geophys. Res.*, *106*(B4), 6673–6682.

Reid, H. F. (1910), The mechanics of the earthquake, in *The California Earthquake of April 18, 1906: Report of the State Investigation Commission*, vol. 2, Carnegie Inst. of Washington, Washington, D. C.

Savage, J. C., R. W. Simpson, and M. H. Murray (1998), Strain accumulation rates in the San Francisco Bay Area, 1972–1989, *J. Geophys. Res.*, *103*(B8), 18,039–18,051.

Savage, J. C., J. L. Svarc, and W. H. Prescott (1999), Geodetic estimates of fault slip rates in the San Francisco Bay Area, *J. Geophys. Res.*, *104*(B3), 4995–5002.

Savage, J. C., W. Gan, W. H. Prescott, and J. L. Svarc (2004), Strain accumulation across the Coast Ranges at the latitude of San Francisco, 1994–2000, *J. Geophys. Res.*, *109*, B03413, doi:10.1029/2003JB002612.

Sawyer, T. L., and J. R. Unruh (2002), Holocene slip rate constraints for the northern Greenville fault, eastern San Francisco Bay Area, California: Implications for the Mt. Diablo restraining stepover model, *Eos Trans. AGU*, *83*(47), Fall Meet. Suppl., Abstract T62F-03.

Schmidt, D. A., R. Bürgmann, R. M. Nadeau, and M. d'Alessio (2005), Distribution of aseismic slip rate on the Hayward fault inferred from seismic and geodetic data, *J. Geophys. Res.*, doi:10.1029/2004JB003397, in press.

Segall, P., R. Bürgmann, and M. V. Matthews (2000), Time dependent triggered afterslip following the 1989 Loma Prieta earthquake, *J. Geophys. Res.*, *105*, 5615–5634.

Shen, Z.-K., et al. (2003), Southern California Earthquake Center crustal motion map version 3.0, http://epicenter.usc.edu/cmm3/.

Sibson, R. H. (1982), Fault zone models, heat flow, and the depth distribution of earthquakes in the continental crust of the United States, *Bull. Seismol. Soc. Am.*, *68*, 1421–1448.

Steblov, G. M., M. G. Kogan, R. W. King, C. H. Scholz, R. Brgmann, and D. I. Frolov (2003), Imprint of the North American plate in Siberia revealed by GPS, *Geophys. Res. Lett.*, *30*(18), 1924, doi:10.1029/2003GL017805.

Thatcher, W., G. Marshall, and M. Lisowski (1997), Resolution of fault slip along the 470-km-long rupture of the great 1906 San Francisco earthquake and its implications, *J. Geophys. Res.*, *102*(B3), 5353–5367.

Thatcher, W., G. R. Foulger, B. R. Julian, J. Svarc, E. Quilty, and G. W. Bawden (1999), Present-day deformation across the Basin and Range province, western United States, *Science*, *283*, 1714–1718.

Townend, J., and M. D. Zoback (2001), Focal mechanism stress inversions in southern California and the strength of the San Andreas fault, in *Proceedings of the Conference on Tectonic Problems of the San Andreas Fault System*, *Stanford Univ. Publ. Geol. Sci.*, *30*, 268–276.

Tse, S. T., and J. R. Rice (1986), Crustal instability in relation to the depth variation of frictional slip properties, *J. Geophys. Res.*, *91*(B9), 9452–9472.

Unruh, J. R., and W. R. Lettis (1998), Kinematics of transpressional deformation in the eastern San Francisco Bay region, California, *Geology*, *26*, 19–22.

Unruh, J. R., and T. L. Sawyer (1997), Assessment of blind seismogenic sources, Livermore Valley, eastern San Francisco Bay Region: Final technical report submitted to the U.S. Geological Survey, National Earthquake Hazards Reduction Program, award 1434-95-g-2611, U.S. Geol. Surv., Reston, Va.

Unruh, J. R., and T. L. Sawyer (1998), Paleoseismic investigation of the northern Greenville fault, eastern San Francisco Bay Area, California: Final technical report submitted to the U.S. Geological Survey, National Earthquake Hazards Reduction Program award 1434-hq-97-gr-03146, U.S. Geol. Surv., Reston, Va.

Unruh, J. R., K. I. Kelson, D. Manaker, and A. Barron (2002), Critical evaluation of the northern termination of the Calaveras fault, eastern San Francisco Bay Area, California, *Rep. 1430*, William Lettis and Assoc., Walnut Creek, Calif.

Wakabayashi, J. (1999), Distribution of displacement on and evolution of a young transform system: The northern San Andreas fault system, California, *J. Geophys. Res.*, *18*(B6), 1245–1274.

Waldhauser, F., and W. L. Ellsworth (2002), Fault structure and mechanics of the Hayward Fault, California, from double-difference earthquake locations, *J. Geophys. Res.*, *107*(B3), 2054, doi:10.1029/2000JB000084.

Wentworth, C. M., and M. D. Zoback (1989), The style of late Cenozoic deformation at the eastern-front of the California Coast Ranges, *Tectonics*, *8*(2), 237–246.

Wernicke, B., and J. K. Snow (1998), Cenozoic tectonism in the central Basin and Range: Motion of the Sierran-Great Valley block, *Int. Geol. Rev.*, *40*(5), 403–410.

Wesnousky, S. G. (1999), Crustal deformation processes and the stability of the Gutenberg-Richter relationship, *Bull. Seismol. Soc. Am.*, *89*(4), 1131–1137.

Williams, C. F. (1996), Temperature and the seismic/aseismic transition: Observations from the 1992 Landers earthquake, *Geophys. Res. Lett.*, *23*(16), 2029–2032.

Williams, C. F. (2003), Implications of the depth of seismicity for the rupture extent of future earthquakes in the San Francisco Bay Area, *U.S. Geol. Survey Open File Rep.*, *03-214*, A1–A16.

Wong, I. G., and R. W. Ely (1983), Historical seismicity and tectonics of the Coast Ranges-Sierra block boundary: Implications to the 1983 Coalinga earthquakes, in *The 1983 Coalinga, California Earthquakes*, edited by J. Bennet and R. Sherburne, *Spec. Publ. Calif. Div. Mines Geol.*, *66*, 89–104.

Working Group on Northern California Earthquake Probabilities (2003), Earthquake probabilities in the San Francisco Bay region: 2002 to 2031, *U.S. Geol. Surv. Open File Rep.*, *03-214*.

R. Bürgmann, I. A. Johanson, and M. H. Murray, Berkeley Seismological Laboratory, Berkeley, CA 94720-4760, USA.

M. A. d'Alessio, U.S. Geological Survey, 345 Middlefield Road, MS 977, Menlo Park, CA 94025-3591, USA. (dalessio@usgs.gov)

D. A. Schmidt, Department of Geological Sciences, University of Oregon, Eugene, OR 97403, USA.